SEDIMENTOLOGY the journal of the International Association of Sedimentologists

Sedimentology (2020) **67**, 2945–2973 doi: 10.1111/sed.12729

Evaluating new fault-controlled hydrothermal dolomitization models: Insights from the Cambrian Dolomite, Western Canadian Sedimentary Basin

ARDIANSYAH KOESHIDAYATULLAH*[1], HILARY CORLETT†, JACK STACEY*, PETER K. SWART‡, ADRIAN BOYCE§, HAMISH ROBERTSON¶, FIONA WHITAKER¶ and CATHY HOLLIS*

**School of Natural Sciences, University of Manchester, Manchester, M13 9PL, UK (E-mail: cathy.hollis@manchester.ac.uk)*

†MacEwan University, Edmonton, AB, T5J 4S2, Canada

‡Rosenstiel School of Marine and Atmospheric Sciences, University of Miami, Coral Gables, FL, 33149, USA

§Scottish Universities Environmental Research Centre, Glasgow, G75 0QF, UK

¶School of Earth Sciences, University of Bristol, Bristol, BS8 1RJ, UK

Associate Editor – Hairuo Qing

ABSTRACT

Fault-controlled hydrothermal dolomitization in tectonically complex basins can occur at any depth and from different fluid compositions, including 'deep-seated', 'crustal' or 'basinal' brines. Nevertheless, many studies have failed to identify the actual source of these fluids, resulting in a gap in our knowledge on the likely source of magnesium of hydrothermal dolomitization. With development of new concepts in hydrothermal dolomitization, the study aims in particular to test the hypothesis that dolomitizing fluids were sourced from either seawater, ultramafic carbonation or a mixture between the two by utilizing the Cambrian Mount Whyte Formation as an example. Here, the large-scale dolostone bodies are fabric-destructive with a range of crystal fabrics, including euhedral replacement (RD1) and anhedral replacement (RD2). Since dolomite is cross-cut by low amplitude stylolites, dolomitization is interpreted to have occurred shortly after deposition, at a very shallow depth (<1 km). At this time, there would have been sufficient porosity in the mudstones for extensive dolomitization to occur, and the necessary high heat flows and faulting associated with Cambrian rifting to transfer hot brines into the near surface. While the $\delta^{18}O_{water}$ and $^{87}Sr/^{86}Sr$ ratios values of RD1 are comparable with Cambrian seawater, RD2 shows higher values in both parameters. Therefore, although aspects of the fluid geochemistry are consistent with dolomitization from seawater, very high fluid temperature and salinity could be suggestive of mixing with another, hydrothermal fluid. The very hot temperature, positive Eu anomaly, enriched metal concentrations, and cogenetic relation with quartz could indicate that hot brines were at least partially sourced from ultramafic rocks, potentially as a result of interaction between the underlying Proterozoic serpentinites and CO_2-rich fluids. This study highlights that large-scale hydrothermal dolostone bodies can form at shallow burial depths via mixing during fluid pulses, providing a potential explanation for the mass balance problem often associated with their genesis.

[1]Present address: Geological Sciences, Stanford University, Stanford, CA, 94305, USA

Keywords Dolomite, fluid mixing, hydrothermal, magnesium, serpentinites, Western Canada Sedimentary Basin.

INTRODUCTION

Dolomitized Palaeozoic carbonate strata in the Western Canada Sedimentary Basin (WCSB) have attracted many studies over the last few decades, particularly within Devonian strata, due to their significance as hydrocarbon reservoirs (Amthor *et al.*, 1994; Mountjoy *et al.*, 1999; Duggan *et al.*, 2001; Packard *et al.*, 2001). Several dolomitization models have been proposed to explain the range of dolomite fabrics observed in these successions, including seepage-reflux, compactional dewatering, burial and fault-controlled hydrothermal dolomitization (HTD) (Aulstead *et al.*, 1988; Qing & Mountjoy, 1994; Machel & Cavell, 1999; Duggan *et al.*, 2001; Packard *et al.*, 2001; Al-Aasm *et al.*, 2002; Davies & Smith, 2006). Many have proposed that dolomitization took place primarily along crustal-scale wrench faults, facilitated by the presence of aquitards (Duggan *et al.*, 2001; Packard *et al.*, 2001; Jeary, 2002; Davies & Smith, 2006); however, the source of fluid or magnesium has not been specifically defined, often cited as 'deep-seated brines', 'crustal-brines' or 'hydrothermal fluids'.

Recent studies have shown that the convection of seawater along fault planes and basal clastic aquifers can explain the formation of fault-related dolomite from hydrothermal fluids (Martin-Martin *et al.*, 2015; Hollis *et al.*, 2017; Al-Ramadan *et al.*, 2019). These models require that faults are open to the sea floor, as often occurs within extensional basins (Hollis *et al.*, 2017; Hirani *et al.*, 2018). Other more recent studies have also invoked fluid interaction with mafic and ultramafic rocks (for example, serpentinized peridotites) as the source of magnesium and demonstrated the thermodynamic viability of ultramafic carbonation to increasing the potency of dolomitization (Lavoie *et al.*, 2014; Falk & Kelemen, 2015; Robertson *et al.*, 2019). These two new ideas have provided a different view of potential sources for water and magnesium in the formation of large-scale HTD bodies that might be appropriate for reconstruction of dolomitization processes in the WCSB.

The dolomitized sequences of Cambrian strata in the Canadian Rocky Mountains provide excellent exposure of fault-controlled dolostone bodies which are easily accessed, allowing for detailed, methodical sampling across the dolostone bodies. Prior studies of the Cambrian (Series 2) Cathedral Formation (Yao & Demicco, 1997; Jeary, 2002; Vandeginste *et al.*, 2005; Powell *et al.*, 2006) have shown that dolomitization involved hydrothermal fluids in the vicinity of the Kicking Horse Rim (Fig. 1A) and surrounding area. These studies invoked a range of models for explaining dolomitization, including post-Silurian topographically-driven fluid (Yao & Demicco, 1997), focused fluid flow of hot and saline brines along the fold thrust belt associated with Devono–Carboniferous Antler Orogeny (Vandeginste *et al.*, 2005), Cambrian-aged Mg-rich brine seeps sourced from Middle Proterozoic magnesite (Powell *et al.*, 2006) and multiple dolomitization events during the Cambrian period (Series 2 to Furongian) when early dolomitization was overprinted by hydrothermal dolomite, producing several hydrobrecciated zones (Jeary, 2002). Of these models, the suggestion by Powell *et al.* (2006) that Middle Proterozoic magnesite sourced dolomitizing brines have received relatively little attention; this is evaluated here with reference to new models of ultramafic carbonation to drive dolomitization.

This study focuses upon the Mount Whyte Formation, which immediately underlies the Cathedral Formation, and which has been remarkably understudied. It was described principally from the area around Whirlpool Point (Fig. 1A) where it is separated from the Cathedral Formation by a shale unit. The Mount Whyte Formation differs in character from the Cathedral Formation because it does not exhibit well-developed zones of brecciation or zebra dolomite textures. It therefore offers an ideal opportunity to evaluate dolomitization processes within the WCSB, since it appears to have a simpler history of dolomitization than the overlying Cathedral Formation. In particular, the study aims to identify: (i) the potential source of magnesium for dolomitization; (ii) the mechanisms that drive the circulation of dolomitizing fluids and timing of dolomitization; and in particular (iii) to assess the potential of ultramafic-derived carbonation as a source of magnesium

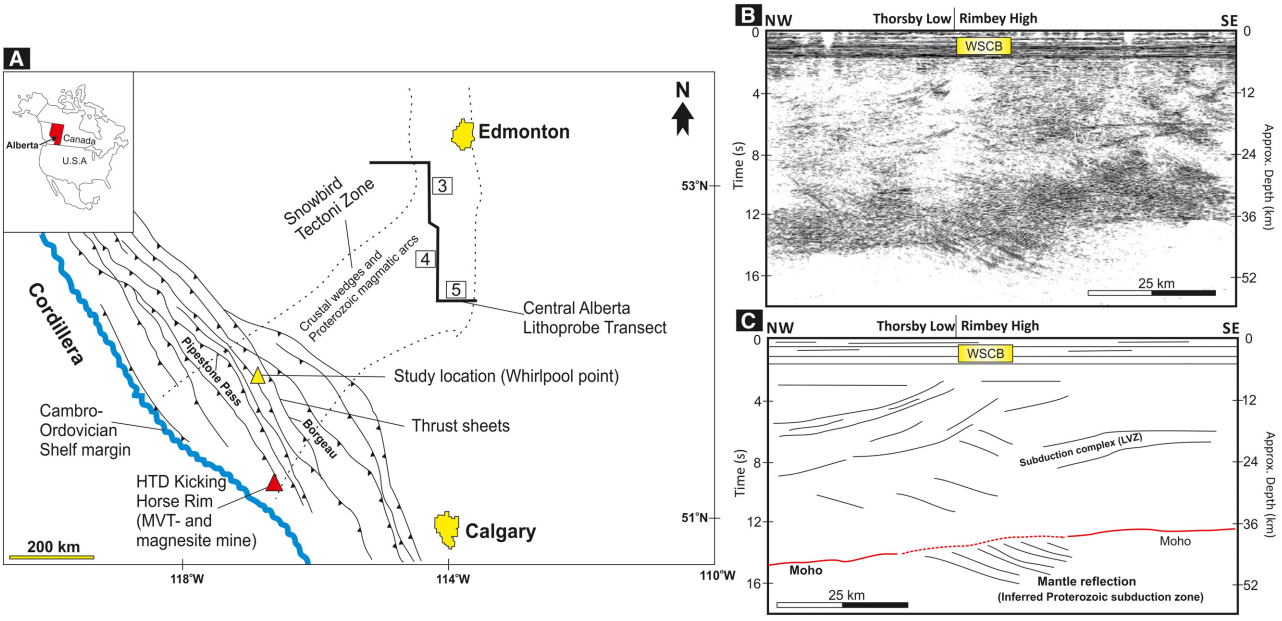

Fig. 1. (A) Map showing structural framework of the Western Canada Sedimentary Basin (WCSB) modified from Davies & Smith, 2006). (B) and (C). Lithoprobe transect ('3' to '5') near the Snowbird Tectonic Zone where it shows the appearance of relict of Proterozoic subduction zone and complex underneath WCSB based on the presence of LVZ (low velocity zones) and dip of the reflection (Eaton & Cassidy, 1996; Van der Velden & Cook, 2005).

for extensive HTD bodies in the Cambrian, and potentially other Palaeozoic, dolomitized successions in the WCSB.

GEOLOGICAL BACKGROUND

The WCSB is a large sedimentary basin, ranging from south-western Manitoba to south-west of Northwest Territories, with a complex tectonic history (Creaney & Allan, 1990; Gabrielse *et al.*, 1991). It is comprised of a sedimentary wedge up to 6 km thick. The sedimentary succession is predominantly composed of Palaeozoic to Mesozoic carbonate rocks, after which it evolved into a clastic-dominated basin, from the Cretaceous until Recent (Creaney & Allan, 1990; Wright *et al.*, 1994). Changes in sedimentation patterns through time were closely associated with the tectonic evolution of the basin, from a rift basin to a passive margin into a foreland basin (Wright *et al.*, 1994). Across the WCSB, the sedimentary sequence overlies a range of Precambrian metamorphic terranes, including a Paleoproterozoic subduction complex, as revealed from lithoprobe transects (Eaton & Cassidy, 1996; Fig. 1B and C). The Terreneuvian succession was deposited in an extensional basin, formed during tectonic reactivation of the Neoproterozoic passive margin (Bond & Kominz, 1984), with preservation of the syn-rift conglomeratic sandstone of the Gog Group (Fig. 2) (Kubli & Simony, 1994). Subsequently, regional subsidence led to several marine transgression–regression cycles (Grand Cycles) during the late-syn rift to post-rift stage, in the Series 2 through to the Furongian period (Slind *et al.*, 1994). This resulted in the growth of several carbonate platforms, including the Mount Whyte, Cathedral and Eldon formations (Aitken, 1997; Powell *et al.*, 2006; Norford, 2012). The Mount Whyte Formation underlies the Cathedral Formation and is considered to be at the base of the second 'Grand' cycle in this region (e.g. Norford, 2012). The Mount Whyte is characterized by interbedded limestone–dolostone and shale in the Front Ranges, where the thickness can reach up to 176 m (Aitken, 1989, 1997; Collom *et al.*, 2009; Fig. 2).

The Mount Whyte Formation is well-exposed at Whirlpool Point (Fig. 1A), where it is bounded by two major north-west/south-east thrust faults; Pipestone Pass to the east and Bourgeau in the west (Fig. 1A). Previous studies have included the limestones and dolostones of the Mount Whyte in this study location into the Cambrian Peyto Formation (Terreneuvian,

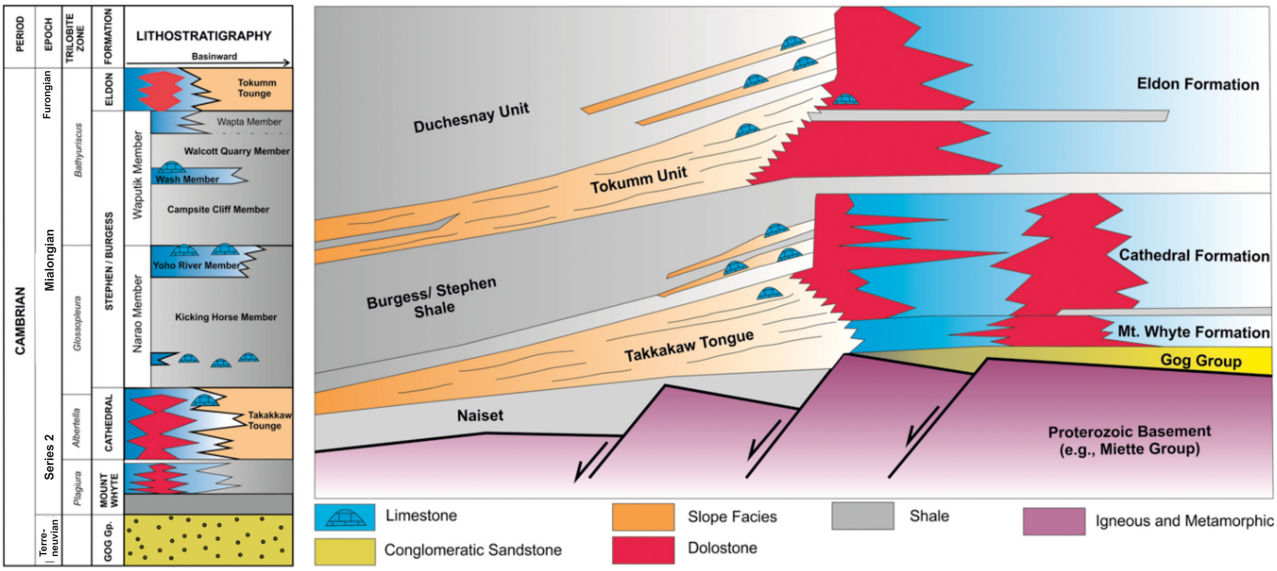

Fig. 2. Schematic Cambrian stratigraphic successions (Series 2 to Furongian) and their platform to basin correlations (modified from Collom *et al.*, 2009). This study included the Gog group sandstone as part of the syn-rift succession while the Mount Whyte Formation belongs to the post-rift sequence. Note the presence of platform-scale dolostone bodies in the three carbonate formations, Mount Whyte, Cathedral and Eldon formations (Aitken, 1978; Yao & Demicco, 1997; Collom *et al.*, 2009). This study focuses on the formation of pervasive dolostone bodies in the Mount Whyte Formation.

Stage 2; Aitken, 1997; Jeary, 2002). However, Aitken (1997) reported the thickness of the Peyto Formation to be only 7.6 m which is significantly thinner than measured at Whirlpool Point (up to 80 m thick; Fig. 3A and B). Because Aitken (1997) does not report explicit measurements of the remaining stratigraphic section in this location, it is possible that the rest of the section (*ca* 70 m) belongs to the Mount Whyte Formation while the lower part belongs to the Peyto Formation.

The reference section of the Mount Whyte Formation is located in the south-west flank of Mount Weed, Mistaya Canyon which is *ca* 50 km south-west from the study location (Aitken, 1997). Here, the Mount Whyte Formation (126 m thick) consists of two members: (i) greenish siltstones of the Weed Member; and (ii) limestone-dominated of the Chephren Member (Aitken, 1997). At Whirlpool Point, the Terreneuvian Gog Group sandstone is partly-exposed (*ca* 10 m thick), comprising medium-grained cross-bedded sandstone to conglomeratic sandstone overlain by greenish siltstones, and is possibly therefore part of the Peyto Formation (see description in Aitken, 1997). Several studies have indicated that the stratigraphic relationship between the Mount Whyte and Peyto formation is unconformable based on the gap in trilobite zones found in both formations (Tremblay, 1996; Aitken, 1997). The Mount Whyte Formation consists of shale and carbonate sediments, comprising stromatolites and thick bedded partially dolomitized mudstones with oncoidal–ooidal grainstone in its upper part (Fig. 3A to D) consistent with deposition in the platform interior (Fig. 3A). It is conformably overlain by the Cathedral Formation. Distinct trilobite faunas, including the Plagiura–Albertalla zone in the Main and Front Ranges indicated that the Mount Whyte and Cathedral formations were deposited during the Series 2 (516.0 to 513.0 Ma; Deiss, 1941; Collom *et al.*, 2009; Fig. 2), which is taken to be the assumed age of the Mount Whyte Formation in this study.

ANALYTICAL METHODOLOGY

A total of 104 samples were collected from the stratigraphic section and various dolostone bodies in the Cambrian Mount Whyte Formation at the Whirlpool Point locality. Thin section analysis was conducted on 74 blue-epoxy resin dyed samples, stained with Alizarin Red and potassium ferrocyanide, using standard petrographic

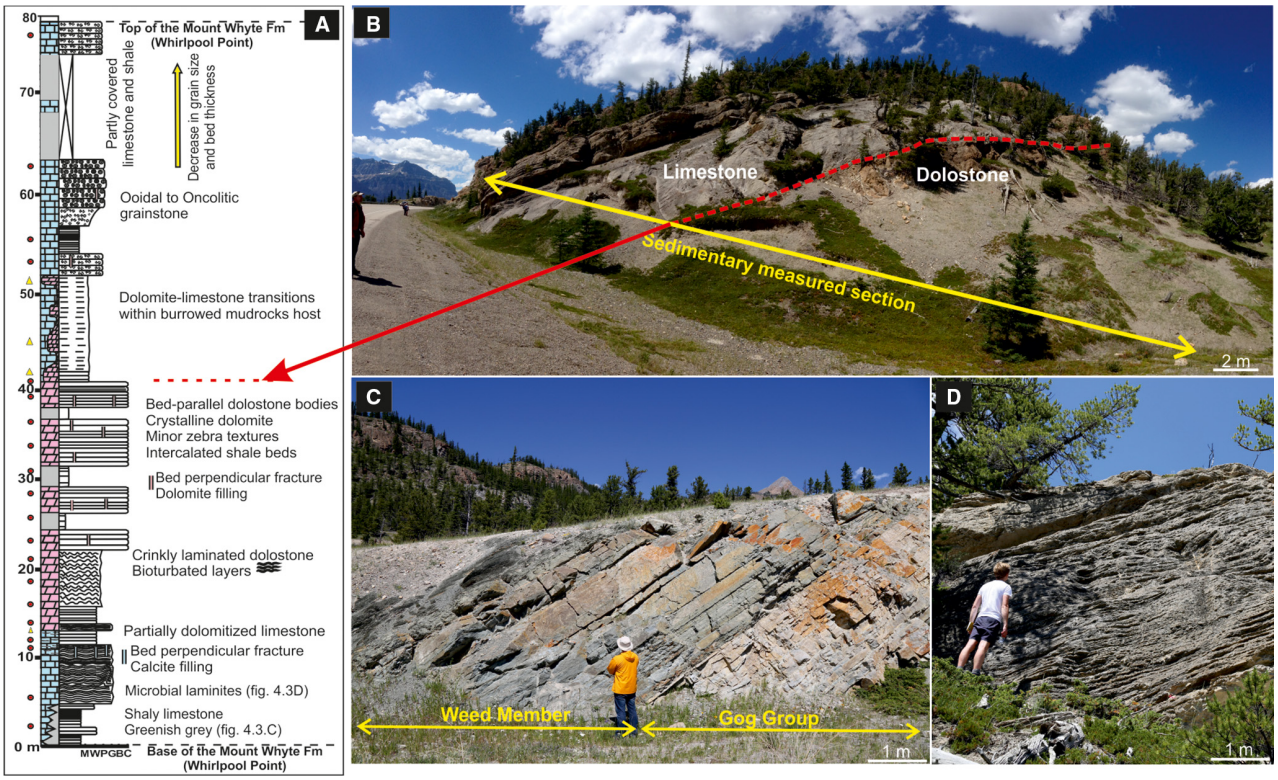

Fig. 3. (A) The measured section of the Mount Whyte Formation showing the detailed lithofacies and the presence of dolostone bodies in the middle part, bounded by mudrocks in the lower part and oncoidal grainstone in the upper part. (B) Outcrop of the Mount Whyte Formation at the Whirlpool Point location. (C) Well-bedded greenish grey siltstones dominate the lower part of the section. Person for scale is *ca* 1.8 m tall. (D) Thinly bedded microbial laminites.

techniques (Dickson, 1966) to qualitatively discriminate between calcite and dolomite. Cathodoluminescence analysis was performed using a [Cambridge Image Technology Limited (CITL), Cambridge, UK] Mk5 Cold cathode stage at the University of Manchester to determine the cement generations and origins. A cold cathode luminescope was used with a beam voltage of *ca* 17 kV and a current of 600 μA.

Scanning electron microscopy (SEM) was performed on selected samples ($n = 16$) by using FEI Quanta FEG 450 (Thermo Fisher Scientific, Waltham, MA, USA) in the Williamson Research Centre, University of Manchester to investigate different mineral microfabrics. The bulk mineralogy of all samples was determined by X-ray Diffraction (XRD) analysis using Bruker D8Advance Diffractometer (Bruker Corporation, Billerica, MA, USA). High-resolution quantitative major, minor and trace elemental analysis was conducted by using Cameca SX 100 Electron Microprobe (EPMA; Cameca, Gennevilliers, France) at the University of Manchester. The analysis was conducted using wavelength dispersive spectrometry (WDS) for Fe, Mn, Ca and Mg, and energy dispersive spectrometry (EDS) for other elements (for example, Ti and Cr) with an accelerating voltage of 15 kV and a beam current of 10 to 20 nA. Replicate measurements of different dolomite crystals show that the analytical precision (1σ) was estimated at $\leq 5\%$.

Nine double-polished, 50 to 100 μm thick sections of selected dolomite samples were selected for fluid inclusion studies. Standard, transmitted-light petrographic analysis was conducted to map the presence of fluid inclusions within the dolomite before detailed examination using the fluid inclusion stage. A heating-freezing stage (LINKAM MDSG 600 system; Linkam Scientific Instruments, Tadworth, UK) attached to a Nikon microscope (Nikon, Tokyo, Japan) at the University of Manchester and a LINKAM THMS-600 stage (−196 to 600°C) coupled to an Olympus BX53 microscope (Olympus, Tokyo, Japan) at the University of Alberta were utilized to perform fluid inclusion analysis, using a standard

method proposed by Goldstein & Reynolds (1994).

For strontium isotope ($^{87}Sr/^{86}Sr$) analysis, 100 to 150 mg of powder of ten whole-rock samples were dissolved a mixture of 1 ml HNO_3 and 1 ml HF in a crucible at 190°C for 48 hours. Strontium produced by reaction between carbonate powder and acid was extracted by using conventional ion exchange procedures using resin cation Bio-Rad AG50 X12 (Baadsgaard, 1987). The resulting Sr isotope ratios were measured using a Triton Plus thermal ionization mass spectrometer (Thermo Fisher Scientific) at the PetroChina Hangzhou Research Institute of Geology, Hangzhou, China. Analytical precision of individual runs is at 0.00005 (2σ). All $^{87}Sr/^{86}Sr$ values were normalized and reported to a NBS-987 standard (0.710253).

For elemental, $\delta^{13}C$ and $\delta^{18}O$, and clumped isotope analyses, thin and thick section counterparts were micro-drilled under a binocular microscope to extract different dolomite fabrics and limestone matrix and cement, in order to avoid mixing of different diagenetic phases and verify the homogeneity of the samples. Trace element (Fe, Mn, Ba and Sr) and rare earth element (REE+Y) concentrations in the samples were analysed using Perkin-Elmer Optima 5300 dual view Inductively Coupled Plasma Atomic Emission Spectroscopy (ICP-AES; Perkin-Elmer, Waltham, MA, USA) and Agilent 7700x Inductively Coupled Plasma Mass Spectrometry (ICP-MS), respectively. A subset of samples used for stable isotope analyses were utilized in both analyses [trace element (n = 15); REEs (n = 10)]. The samples were reacted with 6 M hydrochloric acid (HCl) and 10 ml de-ionized water were added to ensure that total dissolved solids will be less than 0.1%. The liquid samples were then acidified by typically 2% HNO_3 and filtered to remove particles > 0.45 μm. Detection limits for both analyses are as low as 0.01 ppb in solution under the usual operating conditions. The REE concentrations were normalized to both Post-Archean Australian Shales (PAAS) (McLennan, 1989) and chondrite (Anders & Grevesse, 1989), and their anomalies (Ce, Pr, La and Eu) were determined following the methods proposed by Bau & Dulski (1996) and Webb & Kamber (2000).

A total of 42 samples were analysed for their $\delta^{13}C$ and $\delta^{18}O$. The powder samples (5 to 10 mg) (n = 20) were reacted with anhydrous phosphoric acid at 25°C and *ca* 16 h for calcite and 50°C and *ca* 48 h for dolomite (McCrea, 1950) in a carbonate preparation line connected to a VG SIRA 12 gas-source mass spectrometer (Elementar GmbH, Langenselbold, Germany) at the University of Liverpool, UK. An additional 22 samples were analysed at the Scottish Environmental University Research Centre (SUERC), Glasgow using A VG OPTIMA mass spectrometer (Isoprime Limited, Cheadle, UK). A carbonate-phosphoric acid correction factor was applied on the oxygen isotope ratios for both calcite and dolomite by using fractionation factors (i) of 1.01025 (Kim & O'Neil, 1997) and 1.01066 (Rosenbaum & Sheppard, 1986), respectively. All values are reported as delta values with respect to the Vienna PeeDee Belemnite (VPDB) and standardized to NBS-19 and Carrara marble. Average analytical precision and reproducibility for both calcite and dolomite was checked by replicate analysis and it is better than ±0.1‰.

The measurement of clumped isotope on both limestone (n = 5) and dolostone samples (n = 17) was conducted at the Stable Isotope Laboratory, University of Miami by using dual inlet Thermo Scientific 253 ultra-high-resolution isotope ratio mass spectrometers. The CO_2 extraction procedures followed the description of Murray *et al.* (2016) and Swart *et al.* (2016) for the Δ_{47} measurements. For each analysis, 10 to 15 mg of sample was reacted in a common acid bath (103% phosphoric acid at 90°C) for 30 and 45 min on calcite and dolomite, respectively. The yield CO_2 was then frozen in a sealed vessel and transferred into a mass spectrometer where it was measured against a working cryogenically cleaned reference gas. Replicate analyses (two to four times) were performed to correct the error/drift over time and ensure that the results are consistent. The results were then converted to the absolute reference frame (ARF) by following a Carbon Dioxide Equilibrated Scale (CDES) calibration scheme described by Dennis *et al.* (2011). The Δ_{47} value was adjusted and converted to a temperature value without applying acid fractionation factor by using the equation of Staudigel *et al.* (2018) modified for dissolution at 90°C. In addition, during the measurement of clumped isotopes, $\delta^{13}C$ and $\delta^{18}O$ values were measured by calculating the masses 45/44 and 46/44. The correction method proposed by Craig (1957) was followed to correct for the isobaric interferences. As the reaction was conducted at 90°C, the $\delta^{18}O$ value of the dolomite was constantly corrected by –0.8‰ to account for the differential fractionation of CO_2 yielded from dolomite relative to

calcite (Sharma & Clayton, 1965; Land, 1980; Swart *et al.*, 2016). The $^{18}O/^{16}O$ fractionations of calcite–water and dolomite–water published by Kim & O'Neil (1997) and Horita (2014), respectively, were utilized to calculate the oxygen isotopic compositions of parent (i.e. diagenetic fluids ($\delta^{18}Ow$).

RESULTS

Lithofacies

The Gog Group at Whirlpool Point is characterized by the presence of medium to fine grained cross-bedded sandstone. The sandstones are typically cemented by dolomite with the occasional presence of dolomite cemented fractures (Stacey *et al.*, 2017). The Mount Whyte Formation directly overlies the Gog Group and is principally composed of five different lithologies that make up a total succession of *ca* 78 m thickness with both lateral and vertical diagenetic contacts between dolostone (brown) and limestone (grey) (Fig. 3A and B).

1 Grey-greenish shale to siltstone facies occurs only in the lower part of this section and is either well-bedded (centimetre-scale) or structureless (Fig. 3C).

2 Microbial laminites that overlie the siltstone facies and are characterized by *ca* 5 m thick light grey coloured centimetre-scale crinkly laminated mudstone (Fig. 3D).

3 Thinly bedded, burrowed bioclastic wackestone which is mud-supported. The occurrence of dolostone–limestone transitions and preferentially dolomitized burrows within this facies suggests that it was the parent rock of the dolomitized unit (Fig. 4A).

4 Oncoidal packstone to grainstone facies containing oncoid grains (0.2 mm to 2.0 cm in diameter) which remain undolomitized. This unit dominates the upper part of this Mount Whyte section and forms the upper boundary for the dolomitized unit (Fig. 4B).

5 Well-bedded medium to coarse crystalline dolostone that constitutes more than half of the total thickness of the Mount Whyte Formation in the study area. The dolostone is light to dark orange-brown colour with centimetre to metre-scale bedding preserved (Fig. 4C). Thinly bedded shale is often observed intercalated with this dolostone unit. Zebra dolomite fabrics are occasionally associated with this facies but are generally rare (Fig. 4D). North-west/south-east to west–east trending fracture sets cemented by either calcite or dolomite spar are present throughout the outcrop and more pronounced in the dolostone unit (Fig. 4E). In addition, bedding parallel vuggy porosity and low amplitude stylolites can also be recognized in the outcrop (Fig. 4F and G).

Petrography

Three different dolomite fabrics were identified based on their petrographic and cathodoluminescence (CL) characteristics. Visual estimation of their relative volume with respect to other fabrics is also described here.

Replacive dolomite (RD1)

RD1 is a fabric destructive dolomite and characterized by a fine-sized dolomite crystal with relatively unimodal crystal size distribution (50 to 250 μm) (Fig. 5A and B). Under plane polarized light, phase RD1 exhibits planar-e to planar-s textures (*sensu* Sibley & Gregg, 1987) with cloudy, inclusion-rich cores and clear rimmed crystals (Fig. 5A). This phase has distinct CL characteristics, in comparison with other dolomite phases, exhibiting either a dark purple luminescence with no to thin orange bright zones or dull red core or thick, bright orange luminescent zones in the outer rim (Fig. 5C). The presence of RD1 is mostly observed close to dolostone–limestone transitions and occasionally observed as isolated rhombs in the limestone or accumulating along pressure solution seams. Intercrystalline porosity is often found associated with the RD1. This fabric constitutes approximately 25% of the total dolomite volume in the Mount Whyte Formation.

Replacive dolomite (RD2)

This replacive dolomite phase is also strongly fabric destructive and shows a polymodal crystal size distribution (100 to 1000 μm) (Fig. 5D and E). The dolomite crystals exhibit a non-planar texture and closely packed mosaic of subhedral to anhedral crystals with occasional saddle dolomite textures (*sensu* Sibley & Gregg, 1987; Fig. 5E). While this fabric often exhibits coarse crystal sizes (up to 1000 μm), RD2 only rarely shows curved crystal faces and sweeping extinction. RD2 has a characteristic dull red, unzoned CL with some mottled brighter orange-yellow spots in the central part (Fig. 5F). Only very slight variations in CL colour or intensity were

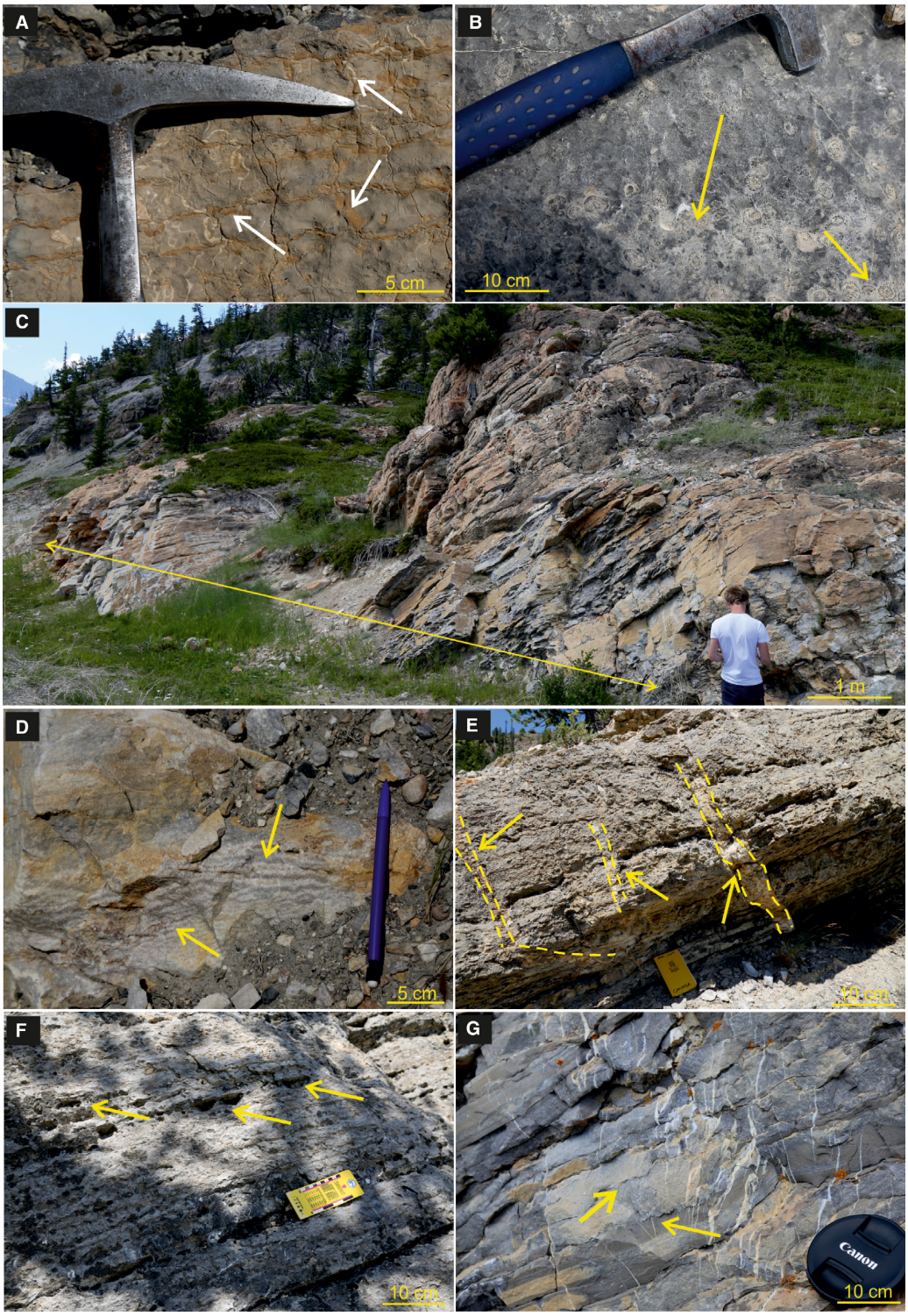

Fig. 4. Outcrop photographs showing different lithofacies characteristics and features observed in the Mount Whyte Formation. (A) Thinly bedded burrowed mudstone which shows preferential dolomitization within the burrows (brown colour; white arrows). (B) Oncoidal grainstone facies with >2 mm sized oncoidal grains (yellow arrows) which dominates the upper part of sedimentary section. (C) Well-bedded, brown dolostone apparent in the middle of the section. (D) Zebra dolomite texture in the Mount Whyte Formation (yellow arrows). (E) Calcite or dolomite cemented fractures observed in the lower part of the Mount Whyte Formation (yellow dashed lines and arrows). (F) and (G) Bedding-parallel vuggy porosity and low amplitude stylolites developed within the dolostone

observed for RD2 from all studied samples. RD2 is the volumetrically most significant dolomite fabric in the Mount Whyte Formation, representing about 65% of dolomitized rock volume.

Saddle dolomite

The saddle dolomite (SD) fabric exhibits undulose extinction, curved crystal cleavage and faces, and megacrystal size (can be >2 mm) which is a typical of saddle-dolomite (*sensu* Radke & Mathis, 1980; Fig. 5G and H). This dolomite fabric is recognized filling interparticle and fracture pore space and is typically related to zebra textures in outcrop. Under CL, SD is compositionally zoned and has bright to dull red luminescent zones and thin to thick bright orange luminescence (Fig. 5I). SD is only present in subordinate amounts, up to 10% of the total dolomite volume.

Host limestone

In the Mount Whyte Formation, the host limestone can be divided into two groups – mud-

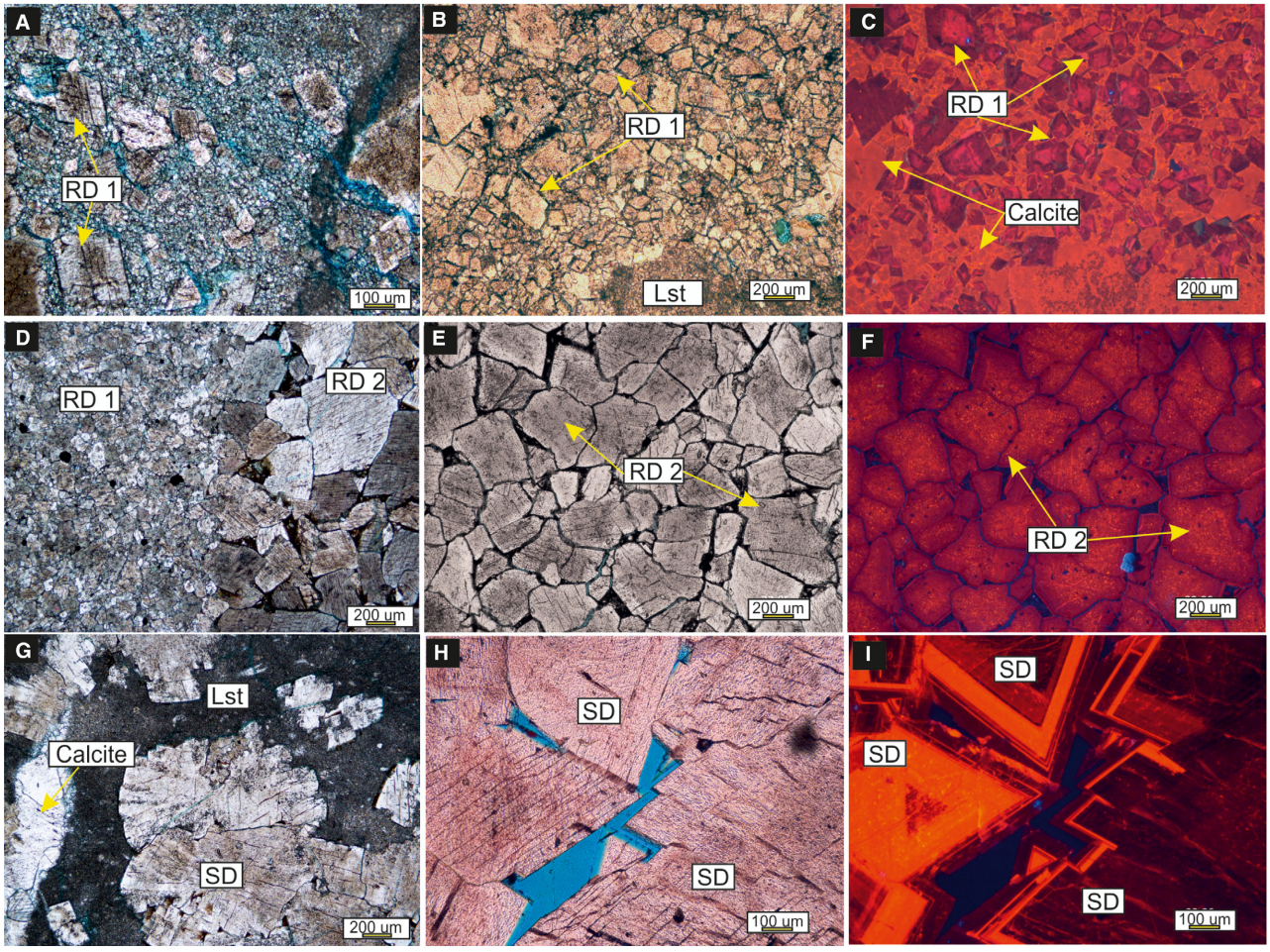

Fig. 5. Thin section images of different dolomite phases present in the Mount Whyte samples. (A) RD1 shows inclusion rich core and clear rim (yellow arrows). (B) Fine-sized crystal of RD1 dolomite fabric with planar-e to planar-s textures (yellow arrows) that partially replaced the host limestone. (C) Cathodoluminescence (CL) character of the RD1, dark to bright red in the centre and thick, purple luminescence in the outer part (yellow arrows). Host limestone is represented by bright orange luminescence (yellow arrows). (D) and (E) RD2 dolomites show coarser crystal size than RD1 and interlocking mosaic of planar-s to anhedral textures. (F) CL image of RD2 of (E) showing dark red luminescence with spots of weak bright orange luminescent. (G) Coarse saddle dolomite crystals filling the pore space between micrites. (H) A typical fracture-filling saddle dolomite with curved crystal faces. (I) CL image of the SD fabric of (H) with dark red to orange luminescence in the core, and multiple zones of bright orange and dull luminescence in the rim.

dominated and grain-dominated facies. Petrographically, the mud-dominated facies are predominantly composed of micrite and a minor amount of microspar (Fig. 6A); in outcrop it is pervasively bioturbated, accentuated by dolomitization of the burrows. Micrite shows bright orange luminescence under CL (Fig. 6B). In contrast, the grain-dominated facies are mainly composed of oncoids and peloids with pervasive marine cements occluding most of the pore space (Fig. 6C and D). The CL characteristic of grain-dominated facies is dull to non-luminescence (Fig. 6E). In the Mount Whyte Formation, the bioturbated mud-dominated facies is preferentially dolomitized whilst the grain-dominated, oncoidal grainstone facies remains as limestone.

Calcite cement

Calcite cement occurs as two different phases: (i) a pore filling phase as observed in the grainstone facies (Fig. 6C); and (ii) a fracture filling phase (Fig. 6A to D). These two phases typically display a similar blocky texture, with crystal sizes ranging from 20 to 500 μm. However, their CL characteristics are different; the pore filling phase is dull to non-luminescence while the fracture-filling phase is either bright orange or

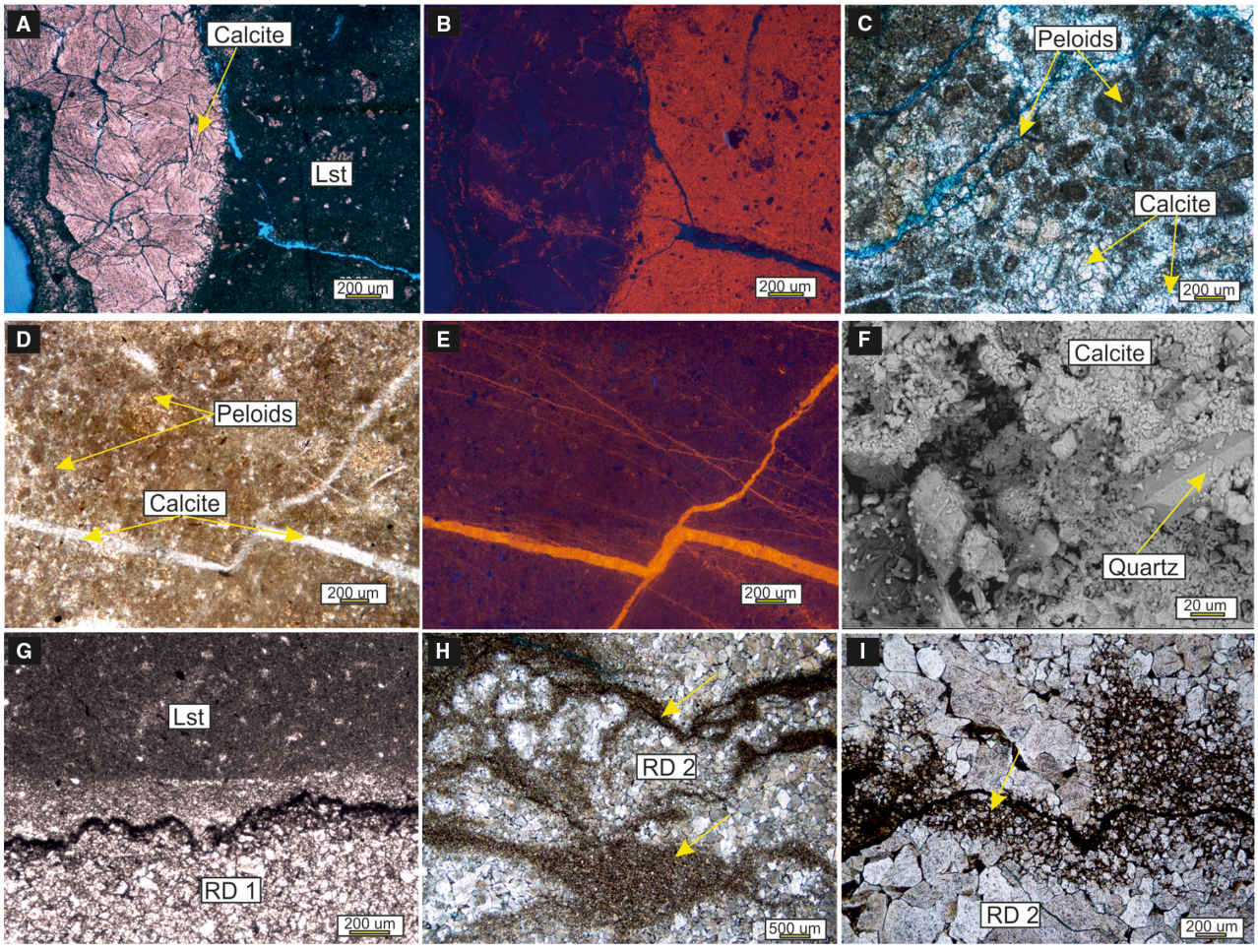

Fig. 6. Thin section images of the Mount Whyte Formation. (A) Mud-supported host limestone with fracture-filling calcite. (B) Cathodoluminescence (CL) image of (A) showing bright orange luminescence for the micrite and non-luminescence for the calcite cement. (C) and (D) Grain-supported, oncoidal to peloidal grainstone. Note the presence of blocky calcite cement filling the pore space between oncoidal grains. (E) Dull and bright orange luminescence of the grainstone and calcite cement. (F) Hexagonal quartz crystals filling the pore space of limestone matrix. (G) Low-amplitude stylolite seams post-dated RD1 fabric. (H) Anastomosing pressure seams with accumulation of fine sized dolomite crystal and residual material. (I) Higher amplitude micro-stylolite cross-cuts the RD2 fabric. Note the presence of insoluble residue along the stylolites.

dull to non-luminescence with no zonation (Fig. 6B to E).

Authigenic quartz
This phase is difficult to identify under transmitted light; however, SEM and XRD analyses (Koeshidayatullah, 2019) reveal the presence of a small percentage of microquartz (<3%) in almost all limestone matrix and dolostone samples (Fig. 6F). Authigenic, hexagonal quartz crystals are observed in the samples using SEM and often occludes macro-porosity and micro-porosity (Fig. 6F).

Stylolite
Low-amplitude stylolites are the dominant pressure solution feature in the Mount Whyte Formation (Fig. 6G). In some cases, these low amplitude stylolites have amalgamated to create an anastomosing pressure seam morphology (Fig. 6H). They are often characterized by the accumulation of less soluble material (for example, dolomite rhombs, organic material) along the surfaces. The dolomite crystals are mainly characterized by microspar-sized crystals (10 to 30 μm) with planar-e to planar-s texture (similar to RD1), embedded within a black matrix (Fig. 6H). Higher amplitude microstylolites are recognized in a few thin sections, characterized by the presence of only minor residual material (Fig. 6I). These different pressure solution morphologies post-date all dolomite fabrics (Fig. 6G and I).

Trace elements

Minor and trace elemental concentrations (Fe, Mn, Sr, Ba, Cr and Ti) were analysed for the two replacive dolomite fabrics (RD1 and RD2) and host limestone (Table 1).

Iron and manganese
Both RD1 and RD2 display significant enrichment of iron (Fe) and manganese (Mn) concentrations when compared to the limestone matrix (Fig. 7A). The mean of Fe and Mn concentrations in the limestone matrix are 2997 ppm and 136 ppm, respectively. In contrast, the mean of Fe and Mn concentrations of RD1 dolomite are *ca* 8225 ppm and *ca* 796 ppm, respectively (Table 1). Similarly, the RD2 fabric also display high mean values of both Fe and Mn concentrations 9053 ppm and 843 ppm, respectively, which were comparable with the RD1.

Strontium and barium
The mean of strontium (Sr) values measured from two different dolomite fabrics (RD1 and RD2) in the Mount Whyte Formation are considerably lower than the host limestone samples, between 28 ppm and 31 ppm, respectively, while the limestone mean value is 808 ppm (Table 1; Fig. 7B). In contrast, the mean of barium (Ba) concentration in the host limestone (246 ppm) is comparable to RD1–RD2, 194 ppm and 226 ppm, respectively (Table 1).

Titanium and chromium
Comparable mean values of Titanium (Ti) concentration in both RD1 and RD2 dolomites are observed in the Mount Whyte Formation, 540 ppm and 482 ppm, respectively (Table 1). This is considerably higher than the limestone, where Ti concentrations in micrites and cements are below the detection limit (<1 ppm). Similarly, no values can be obtained for the chromium (Cr) concentration in the host limestone samples whereas the RD1 and RD2 dolomites show mean values between 50 and 62 ppm (Table 1).

Rare earth elements

Distribution of rare earth elements (REEs)+Y in the two dolomite fabrics and host limestone are presented in Table 2 and Fig. 8 and described below.

Replacive dolomite (RD1)
The mean of total content of REEs (ΣREE) for this dolomite phase is 6.8 ppm. The mean of ΣLREE (6.6 ppm) displays an enrichment in comparison with the ΣHREE (0.25 ppm). The mean ratio between Y/Ho is 21.8 (Table 2). Positive Eu anomalies ($Eu/Eu^* = [Eu/(0.67Sm + 0.33\ Tb]_{SN}$) range from 1.8 to 3.2 and are clearly illustrated in both PAAS and chondrite normalized REE profiles (Fig. 8A and B). There is no correlation between Ba and Eu suggesting the absence of Ba interference during the REE analysis (Fig. 8C). In addition, the calculation of both Ce anomalies ($Ce/Ce^* = [Ce/(0.5\ La + 0.5\ Pr]_{SN}$) and Pr anomalies ($Pr/Pr^* = [Pr/(0.5\ Ce + 0.5\ Nd]_{SN}$) display values close to 1 (Fig. 8D).

Replacive dolomite (RD2)
The RD2 phase REE profile displays a mean of ΣREE (14.7 ppm) that is almost three times

Table 1. Minor and trace elements, and stable isotopic compositions of the host limestone and different dolomite phases.

Phase	Fe (ppm)	Mn (ppm)	Sr (ppm)	Ba (ppm	Ti (ppm)	Cr (ppm)	$^{13}C_{VPDB}$ (‰)	$^{18}O_{VPDB}$ (‰)
Host Limestone (n = 15)								
Minimum	1150	44	428	171	<LOD	<LOD	−1.1	−13.9
Maximum	5201	274	1116	337			−0.4	−7.9
Mean	2997	136	808	246			−0.7	−11.3
SD	1074	52	281	68			0.3	1.2
Replacive Dolomite 1 (RD1) (n = 20)								
Minimum	6920	525	22	133	410	46	−0.9	−17.8
Maximum	9419	927	42	252	777	80	0.1	−14.1
Mean	8225	796	31	194	540	62	−0.6	−16.1
SD	1021	167	8	49	152	14	0.4	1.5
Replacive Dolomite 2 (RD2) (n = 14)								
Minimum	6928	559	14	138	131	32	−0.9	−17.5
Maximum	15352	1309	50	339	859	85	−0.1	−14.1
Mean	9053	843	28	226	482	50	−0.7	−16.1
SD	3577	309	15	82	297	22	0.3	1.4

higher than the RD1. There is a similar enrichment pattern of ΣLREE (mean: 14.1 ppm) with respect to the ΣHREE (mean: 0.64 ppm), and a comparable trend between RD1 and RD2 with positive anomalies of Eu (Eu/Eu* > 1) (Fig. 8A and B) and non-anomalous Ce and Pr (Ce/Ce* and Pr/Pr* *ca* 1) (Fig. 8D). The mean of Y/Ho ratio of this dolomite fabric is 26.9 (Table 2).

Host limestone

The host limestone shows a slightly lower ΣREE mean value (5.9 ppm) than the RD1 and RD2, which have mean values of ΣLREE and ΣHREE of 5.6 ppm and 0.33 ppm, respectively. The mean value of Y/Ho ratio of the host limestone is 27.8 (Table 2). Normal (i.e. non-anomalous) Eu (Eu/Eu* *ca* 1), Ce, Pr anomalies (Ce/Ce* and Pr/Pr* *ca* 1) are also observed in the PAAS-normalized profile of the host limestone samples, they are lower than the two different fabrics (RD1 and RD2) (Fig. 8A to D).

Stable isotope data

Carbon ($\delta^{13}C$) and oxygen ($\delta^{18}O$) isotope data are presented in Tables 1 and 3. The mean value of $\delta^{13}C$ of limestone ($\delta^{13}C_{calcite)}$ and dolostone ($\delta^{13}C_{dolomite}$) are similar, −0.7‰ and −0.65‰ VPDB, respectively. In contrast the mean of $\delta^{18}O_{dolomite}$ values of the three dolomite fabrics are all more negative than the limestones ($\delta^{18}O_{calcite}$): in descending order, (i) host limestones (mean: −11.5‰ VPDB); (ii) SD (zebra) dolomites (mean: −14.2‰ VPDB); (iii) RD2 dolomites (mean: −15.8‰ VPDB); and (iv) RD1 fabric (mean: −16.0‰ VPDB). The $\delta^{13}C_{dolomite}$ values fall within the range of Cambrian seawater while the values of $\delta^{18}O_{dolomite}$, even though tightly clustered (vary in the range of 2 to 3‰ VPDB), are much more negative compared to dolomite precipitated in equilibrium with Cambrian seawater (−6 to 0‰ SMOW) (Veizer & Prokoph, 2015; Ryb & Eiler, 2018) (Fig. 9).

Fluid inclusion microthermometry

Fluid inclusion microthermometry was conducted in dolomite fabrics RD1, RD2 and SD (Table 3). The primary fluid inclusions (i.e. within growth zones or parallel to the crystal facet) in these samples are usually very small in size (4 to 8 μm) (Fig. 10A to C), but a small number of unusually large fluid inclusions (up to 20 μm) can also be observed (Fig. 10B). The majority of the fluid inclusions observed in this study are two-phase with 10 to 20% vapour–liquid ratio. Statistically, the homogenisation temperature (Th) in the dolomite samples can be grouped into (Fig. 10): (i) RD1 (mean: 124°C); (ii) RD2 in the middle part (mean: 147°C); (iii) RD2 in the core of the body (mean: 181°C) and (iv) saddle dolomite cement associated with either fracture or zebra dolomite fabrics (mean: 181°C). The Th of the smaller fluid inclusions cannot be obtained due to the equipment limitation. Analyses of

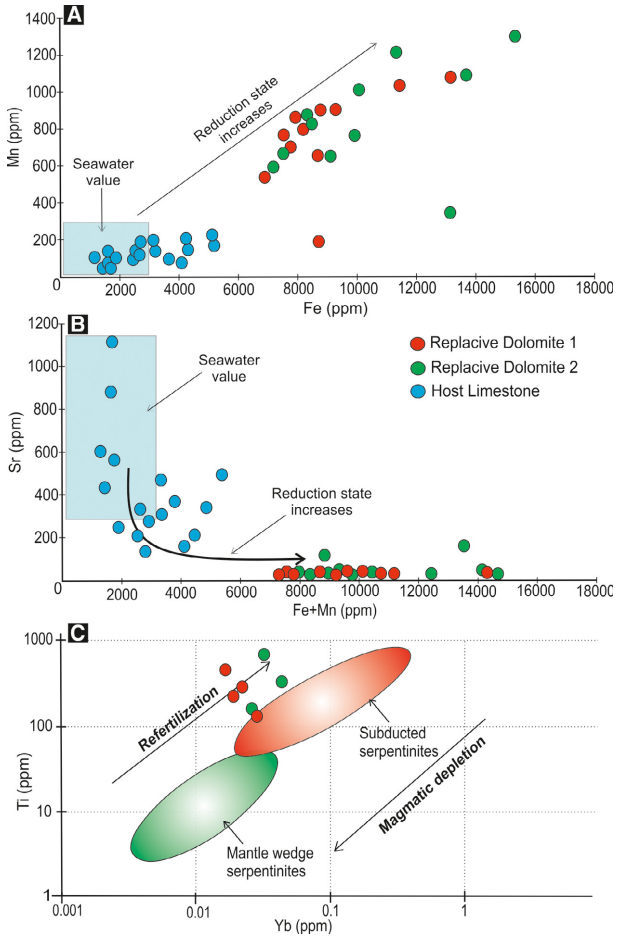

Fig. 7. Trace elements cross-plots. (A) Enrichment of Fe and Mn concentrations in the two dolomite fabrics compared to the host limestone and seawater values (Veizer, 1983). (B) Contrasting Sr and Fe+Mn concentrations between the host limestone and different dolomite phases. The Sr content of dolomites is significantly lower than the expected seawater values (Veizer, 1983). (C) Cross-plot between Titanium (Ti) and Ytterbium (Yb) of different dolomite phases. The red and green fields show different signatures of serpentines based on Deschamps *et al.* (2013).

the melting temperature (Tm) of different samples were also attempted, however none of the large fluid inclusions (10 to 20 μm) were frozen during the analysis (up to −180°C).

Strontium isotope analysis

Strontium isotope analysis was conducted on eight dolomite samples and two whole rock limestone samples. Overall, the values show two different populations with the dolomite samples

Table 2. Unnormalized REE+Y for the host limestone and two dolomite phases in the Mount Whyte Formation. All values are measured in ppm.

Phase	La	Ce	Pr	Nd	Sm	Eu	Gd	Tb	Dy	Ho	Er	Tm	Yb	Lu	Y	Y/Ho	ΣREE	ΣLREE	ΣHREE
Host limestone	1.003	2.026	0.220	0.764	0.125	0.032	0.111	0.015	0.073	0.016	0.036	0.004	0.033	0.052	0.390	24.978	4.511	4.281	0.230
	0.862	2.330	0.293	1.030	0.226	0.064	0.247	0.031	0.153	0.026	0.072	0.009	0.062	0.035	0.758	28.895	5.439	5.052	0.390
	1.635	3.551	0.410	1.441	0.255	0.053	0.206	0.025	0.142	0.028	0.089	0.009	0.072	0.008	0.828	29.400	7.925	7.551	0.370
Mean	1.167	2.636	0.307	1.078	0.202	0.050	0.188	0.023	0.123	0.023	0.066	0.008	0.056	0.032	0.659	27.758	5.958	5.628	0.330
Replacive dolomite (1)	0.786	1.713	0.196	0.652	0.159	0.051	0.145	0.017	0.076	0.016	0.040	0.005	0.032	0.008	0.300	18.646	3.894	3.701	0.190
	1.637	4.003	0.455	1.553	0.268	0.090	0.223	0.031	0.119	0.024	0.063	0.008	0.062	0.031	0.627	25.828	8.567	8.229	0.340
	1.601	3.234	0.330	1.087	0.235	0.134	0.200	0.022	0.101	0.019	0.057	0.006	0.044	0.006	0.363	18.772	7.077	6.821	0.260
	1.527	3.051	0.307	1.019	0.235	0.130	0.194	0.020	0.097	0.016	0.052	0.006	0.042	0.005	0.341	20.785	6.700	6.463	0.240
	1.659	3.758	0.411	1.376	0.226	0.104	0.196	0.019	0.092	0.018	0.057	0.005	0.036	0.008	0.439	24.852	7.968	7.732	0.240
Mean	1.442	3.152	0.340	1.137	0.225	0.102	0.192	0.022	0.097	0.019	0.054	0.006	0.043	0.012	0.414	21.777	6.841	6.589	0.252
Replacive dolomite 2 (RD2)	2.978	7.080	0.797	2.713	0.424	0.121	0.374	0.048	0.207	0.044	0.128	0.015	0.093	0.036	1.179	26.511	15.058	14.487	0.570
	3.204	8.433	1.036	3.655	0.641	0.166	0.522	0.066	0.304	0.059	0.177	0.022	0.139	0.028	1.684	28.480	18.452	17.658	0.790
	2.141	4.669	0.564	2.050	0.386	0.085	0.283	0.037	0.199	0.042	0.112	0.015	0.097	0.044	1.094	25.901	10.723	10.178	0.540
Mean	2.774	6.728	0.799	2.806	0.484	0.124	0.393	0.050	0.236	0.049	0.139	0.017	0.110	0.036	1.319	26.964	14.744	14.108	0.637

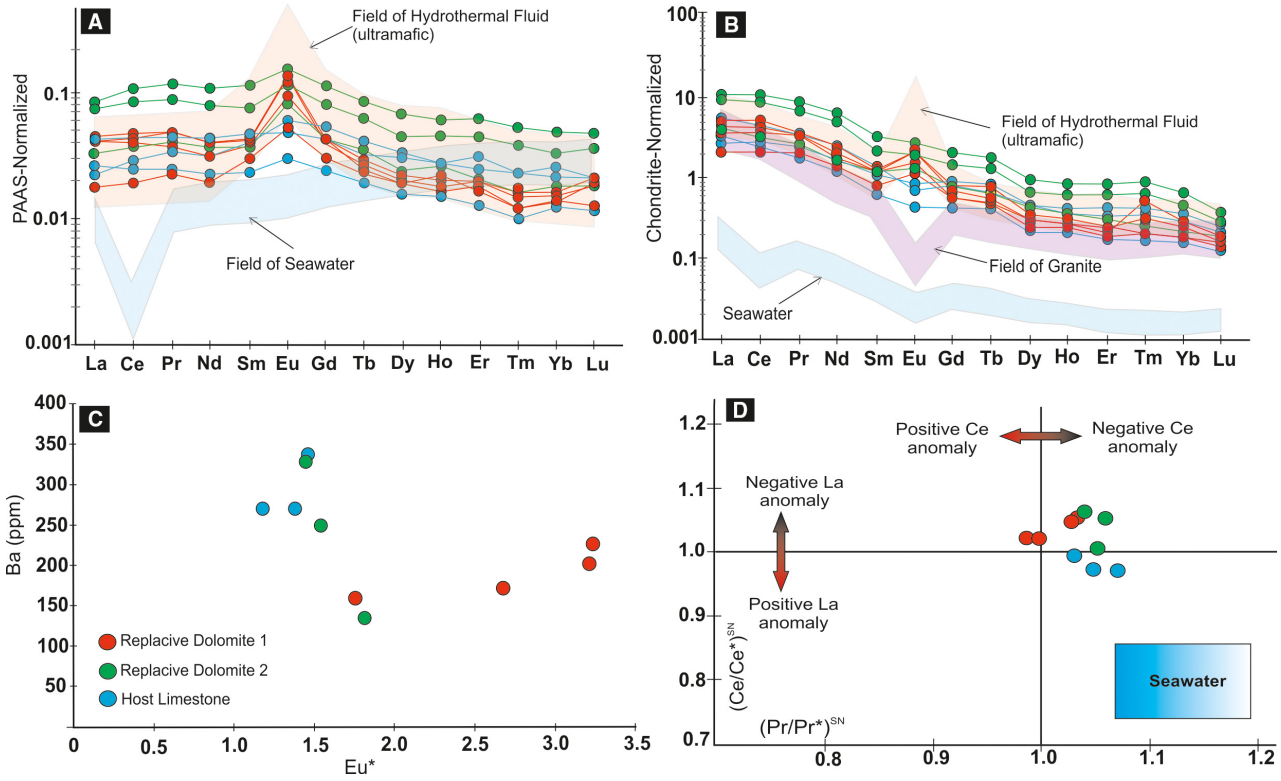

Fig. 8. Rare earth element (REE) profiles in the Mount Whyte Formation. (A) Post Archean Australian Shale (PAAS)-normalized REE profile of different dolomite fabrics (RD1 and RD2) and host limestones. The seawater REE profile is from James *et al.* (1995) while the ultramafic-hosted hydrothermal fluid and granite REE profiles are from Douville *et al.* (2002) and Ishihara *et al.* (2008), respectively. (B) Chondrite-normalized REE profile of different dolomite fabrics (RD1 and RD2) and host limestones. (C) Cross-plot between Ba and Eu anomaly. (D) Cross-plot between Ce anomaly and Pr anomaly showing all the values are within a narrow range and close to 1 (non-anomalous).

exhibiting higher $^{87}Sr/^{86}Sr$ values than the host limestone (Table 3). The mean values are: (i) RD1 fabric (mean: 0.7098); (ii) RD2 fabric (mean: 0.7107); (iii) SD fabric (0.7114); and (iv) host limestone (mean: 0.7095). While the mean of $^{87}Sr/^{86}Sr$ value of limestone is close to the postulated $^{87}Sr/^{86}Sr$ value of Cambrian seawater (Series 2; 0.7090 to 0.7095; Montanez *et al.*, 1996), the $^{87}Sr/^{86}Sr$ values of dolomite samples are much higher than the seawater.

Clumped isotope thermometry and oxygen isotope of fluid

The clumped isotope values (Δ_{47}) of Mount Whyte dolomite samples range from 0.308‰ to 0.452‰ (mean: 0.355‰) (Table 3). The limestone samples show a narrow range of Δ_{47} values from 0.323‰ to 0.385‰ (mean: 0.365‰). For dolomites, the Δ_{47} ratios can be differentiated into four groups, primarily based on their position within dolostone bodies (Table 3): (i) euhedral–subhedral replacive dolomite (RD1) shows Δ_{47} values ranging from 0.333 to 0.452‰; (ii) subhedral–anhedral dolomite (RD2) observed in the core of dolostone bodies exhibits a range of values from 0.308 to 0.363‰; (iii) RD2 fabric observed closer to the reaction front (mid-point) displays a narrower range of values than the RD1 and RD2 at the core, 0.345 to 0.369‰; and (iv) the Δ_{47} values of the saddle dolomite phase (SD) observed within a zebra texture shows two distinct groups (mean: 0.387‰ and 0.352‰). In general, the mean of Δ_{47} values of the replacive dolomite (RD1) observed near the margin of the bodies (mean: 0.376‰) are higher than values obtained in the main dolostone bodies (RD2) (mean: 0.349‰). The results of clumped isotope temperature determination show a relatively good agreement with the temperature range observed in fluid inclusion microthermometry results. However, most of the temperature values

Table 3. Results from stable, clumped and strontium isotopes, and fluid inclusion analyses.

Phase	$^{13}C_{VPDB}$ (‰)	$^{18}O_{VPDB}$ (‰)	Δ47-RF (CDES @ 90°C)*	±1 SD (‰)	$T\Delta_{47}$ (°C) *	$^{18}O_{water}$ (SMOW)	Th (°C)	$^{87}Sr/^{86}Sr$
Host limestone (n = 5)								
Min	−0.3	−11.7	0.324	0.0019	146	8.2	–	0.709384
Max	−0.9	−8.9	0.385	0.023	185	12.6	–	0.709691
Mean	−0.7	−10.6	0.365	0.013	164	10.3	–	0.709538
SD	0.2	1.2	0.025	0.009	15.9	1.8	–	0.000125
Replacive dolomite 1 (margin) (n = 4)								
Min	−0.8	−16.7	0.333	0.018	93	−5.9	91	0.709781
Max	−0.3	−15.1	0.452	0.025	173	3.1	153	0.709851
Mean	0.1	−15.8	0.376	0.021	146	0.4	124	0.709816
SD	0.4	0.7	0.049	0.003	21.8	2.4	25.3	0.000029
Replacive dolomite 2 (core) (n = 4)								
Min	−0.9	−14.9	0.308	0.007	174	3.2	161	0.709660
Max	0.3	−16.7	0.363	0.016	239	6.9	218	0.712240
Mean	−0.4	−15.5	0.333	0.010	205	5.1	181	0.710699
SD	0.5	0.7	0.022	0.004	19.2	1.2	23.6	0.001060
Replacive dolomite 2 (mid body) (n = 4)								
Min	−0.8	−16.3	0.345	0.008	130	−0.3	121	
Max	−0.4	−15.1	0.369	0.018	185	4.1	189	
Mean	−0.6	−15.6	0.365	0.012	164	2.3	147	
SD	0.2	0.5	0.010	0.004	16.5	1.3	28.0	
Saddle dolomite (zebra) (n = 2)								
Min	−1.1	−14.5	0.339	0.010	131	2.6	110	0.711112
Max	−0.4	−13.9	0.398	0.012	192	5.2	245	0.711633
Mean	−0.7	−14.2	0.369	0.011	160	3.8	181	0.711373
SD	0.3	0.2	0.024	0.001	24.9	1.1	55.1	0.000213

* Calculation following Staudigel *et al.* (2018).

obtained from clumped isotopes are higher than the fluid inclusion (Table 3 and Fig. 11). The calculated mean of $\delta^{18}O_{water}$ of the different dolomite phases can be also grouped into: (i) RD1, +1.2‰; (ii) RD2 closer to the reaction fronts (middle body), +2.3‰; (iii) RD2 in the core of the body, +5.1‰; and (iv) SD phase (zebra dolomite), +3.8‰. Much more positive calculated mean of $\delta^{18}O_{water}$ values are estimated from the host limestone, +10.3‰.

INTERPRETATION AND DISCUSSION

Diagenetic environments and paragenesis

Outcrop observations and petrographic studies are used to define the relative timing of diagenetic features (Figs 5 and 6). The earliest diagenetic phases include micritization of skeletal and non-skeletal grains and precipitation of blocky calcite cementation. This blocky calcite cement preserves an open, uncompacted texture, filling the primary interparticle pore spaces between oncoidal grains (Fig. 6C and D). It is therefore interpreted as marine, with the blocky texture reflecting precipitation from low-magnesium calcite seawater during the Cambrian (Horita *et al.*, 2002). High concentrations of Sr and low concentrations of Mn and Fe alongside seawater-like $\delta^{13}O_{calcite}$ values (mean: −0.7‰ VPDB; Figs 7 and 9) support this interpretation.

Near-surface, marine diagenesis may also be inferred from the presence of burrow-selective dolomitization in the host limestone (Fig. 4A), suggestive of microbially-mediated dolomitization during bioturbation (e.g. Gingras *et al.*, 2004; Corlett & Jones, 2012). However, the original geochemical signatures of the burrow-selective dolomitization appear to have been altered during subsequent high-temperature dolomitization events, evidenced by more negative $\delta^{18}O_{dolomite}$, elevated Fe-Mn concentrations, $\delta^{18}O_{water}$ and temperature than would be

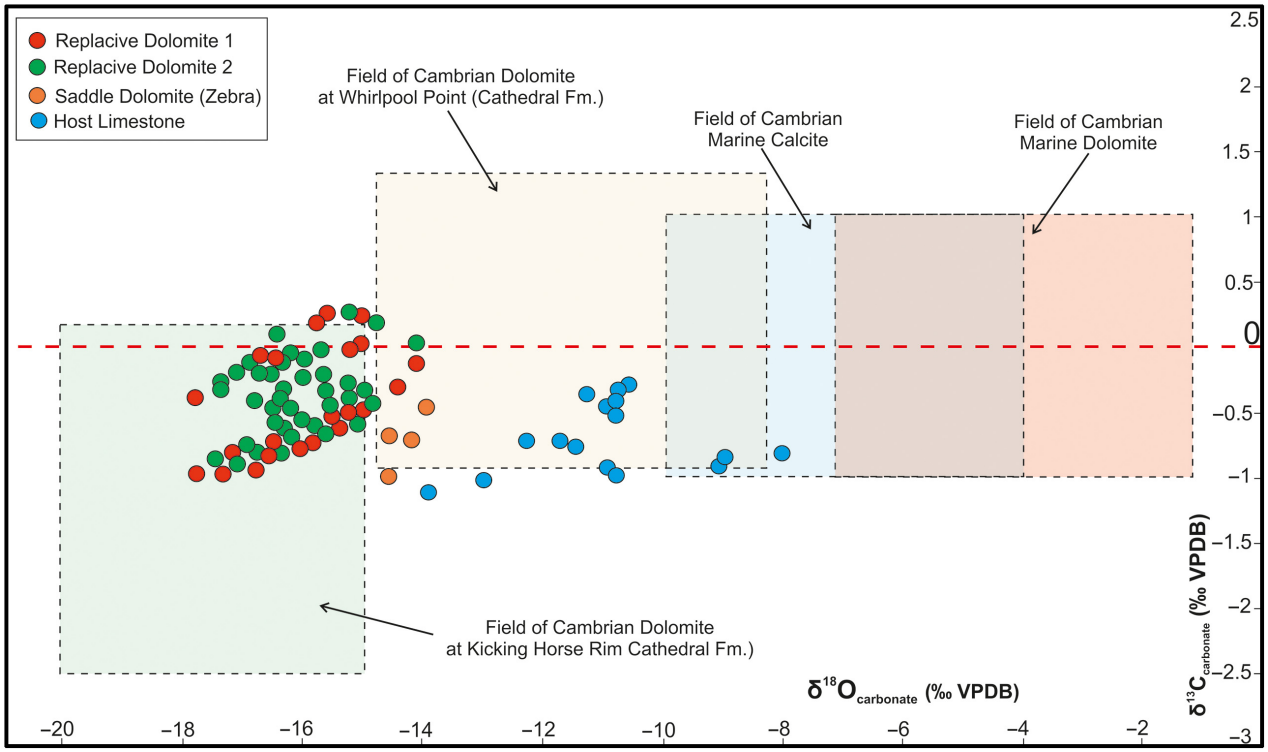

Fig. 9. Cross-plot between $\delta^{13}C$ and $\delta^{18}O$ values of the Mount Whyte formation comparing them to the expected Cambrian marine limestone and dolostone (Veizer & Prokoph, 2015; Henkes *et al.*, 2018; Ryb & Eiler, 2018) and the overlying Cambrian Cathedral dolomites at Whirlpool Point and Kicking Horse locations (Yao & Demicco, 1997; Jeary, 2002; Vandeginste *et al.*, 2005). Note that the dolomite $\delta^{18}O$ values of the Mount Whyte Formation are more negative than the host limestone counterparts and Cathedral dolomites at Whirlpool Point.

expected from near-surface, microbially mediated dolomitization (Table 3).

Subsequent burial diagenetic events can be divided into two stages; (i) shallow burial (<1 km) and (ii) deep burial (1 to 6 km). Mechanical compaction can only be observed in some parts of the host limestone facies and is notably absent in the grain-supported facies due to the presence of marine cements which appear to have inhibited compaction. The cross-cutting relationship between low amplitude stylolites and dolomite suggests that dolomitization predated stylolitization (Fig. 6G to I). Machel (2004) and Beaudoin *et al.* (2016) suggested that formation of stylolites in mud-dominated carbonate facies can begin at between 500 m to 1 km, implying that dolomitization occurred at depths of less than 1 km, although the possibility of slightly greater depths for the onset of stylolitization cannot be ruled out. Dolomitization produced fabric-destructive dolomites (RD1, RD2 and SD), which are typically associated with formation above the critical roughening temperature of 55°C (Sibley & Gregg, 1987). All fabrics exhibit high concentrations of Fe and Mn, and low Sr concentrations (Table 1) and depleted $\delta^{18}O_{dolomite}$ (mean: −15.8‰ VPDB) which suggests dolomitization from isotopically enriched fluids ($\delta^{18}O_{water}$ mean: +5.1‰ SMOW) compared to Cambrian seawater at surface temperature (−7 to −1‰ VPDB; Swart, 2015; Veizer & Prokoph, 2015; Ryb & Eiler, 2018). In addition, both fluid inclusion (Tm) and Δ_{47} temperatures are very high (up to 235°C). Water/rock ratios (W/R), calculated following the method proposed by Banner & Hanson (1990) for the different dolomite fabrics (using the original composition of $\delta^{18}O_{rock}$, $\delta^{18}O_{fluid}$ and crystallization temperature) were moderately high, particularly for RD1 (0.3 to >10 W/R, depending on the Cambrian seawater values) (Fig. 11B and C).

Burial history of Mount Whyte Formation

Burial history reconstruction indicates continuous burial of Cambrian strata, depending on their location, that can reach up to approximately 4 km, with increasing burial depths towards the

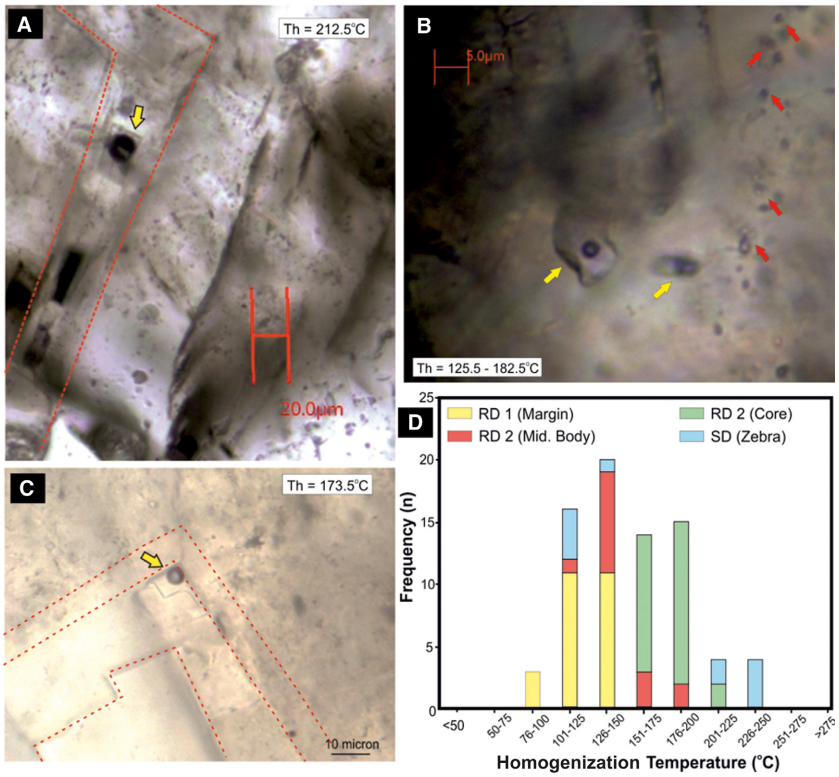

Fig. 10. Fluid inclusion study of the Mount Whyte Formation. (A) to (C) Different examples of two-phase fluid inclusions in the Mount Whyte dolomites and their corresponding homogenization temperature (Th °C). Note that most of the primary fluid inclusions are small in size (<10 μm). (D) Histogram of homogenization temperature of different phases of dolomites.

Mountain Ranges during the onset of the Laramide Orogeny in the Jurassic–Cretaceous (Wright *et al.*, 1994; Jeary, 2002). Fracturing and cementation by bright orange luminescence calcite and creation of high amplitude micro-stylolites, which all cross-cut the dolostone fabrics, could have occurred at any point from the Devonian onward, when burial depths exceed 1 km.

To date, the maximum burial depth of the Mount Whyte Formation in this part of the basin has still not been confidently determined. Although $\delta^{13}C_{calcite}$ values and trace elemental concentrations of micrite and marine calcite cements are within the expected range of Cambrian marine values, some of the geochemical signals of (for example, light $\delta^{18}O_{calcite}$, high Δ_{47} -derived temperature and the absence of a negative Ce anomaly) are inconsistent with seawater precipitation. Water/rock ratios are very low, calculated to range from 0.05 to 0.3, depending on the original values of Cambrian seawater (Fig. 11B and C). Banner & Hanson (1990) suggested that modification of REE would require high water/rock ratios, but Wallace *et al.* (2017) suggested that Cambrian seawater did not have a Ce anomaly since seawater was not as oxygenated as it is today. It is possible therefore that $\delta^{18}O_{calcite}$ and Δ_{47} signatures were altered during burial recrystallization, which usually occurs within a semi-closed (rock-buffered) system and could occur during deep burial (Brand & Veizer, 1980; Czerniakowski *et al.*, 1984; Banner & Hanson, 1990). In other words, the recorded Δ_{47} ratios may reflect solid-state reordering during geothermal heating or rock-buffered crystallization during burial which can be used to approximate the burial depth of the limestone (Ghosh *et al.*, 2006; Passey & Henkes, 2012; Winkelstern & Lohmann, 2016; Lawson *et al.*, 2018).

Cambrian limestone formed under ambient seawater conditions should display high Δ_{47} values (0.58 to 0.57; 30–35°C using Staudigel *et al.* (2018) temperature conversion), but instead they show much lower values (mean: 0.365; mean: 164°C using similar temperature conversion). Winkelstern & Lohmann (2016) suggested that a threshold of Δ_{47} calcite reordering under rock-buffered diagenesis system in micrite-dominated rocks could occur at 70°C [<2 km if using normal geothermal gradient; 25°C/km (Weides & Majorowicz, 2014) and 35°C surface temperature (Henkes *et al.*, 2018)]. The Δ_{47} temperatures of the Mount Whyte micritic limestones range

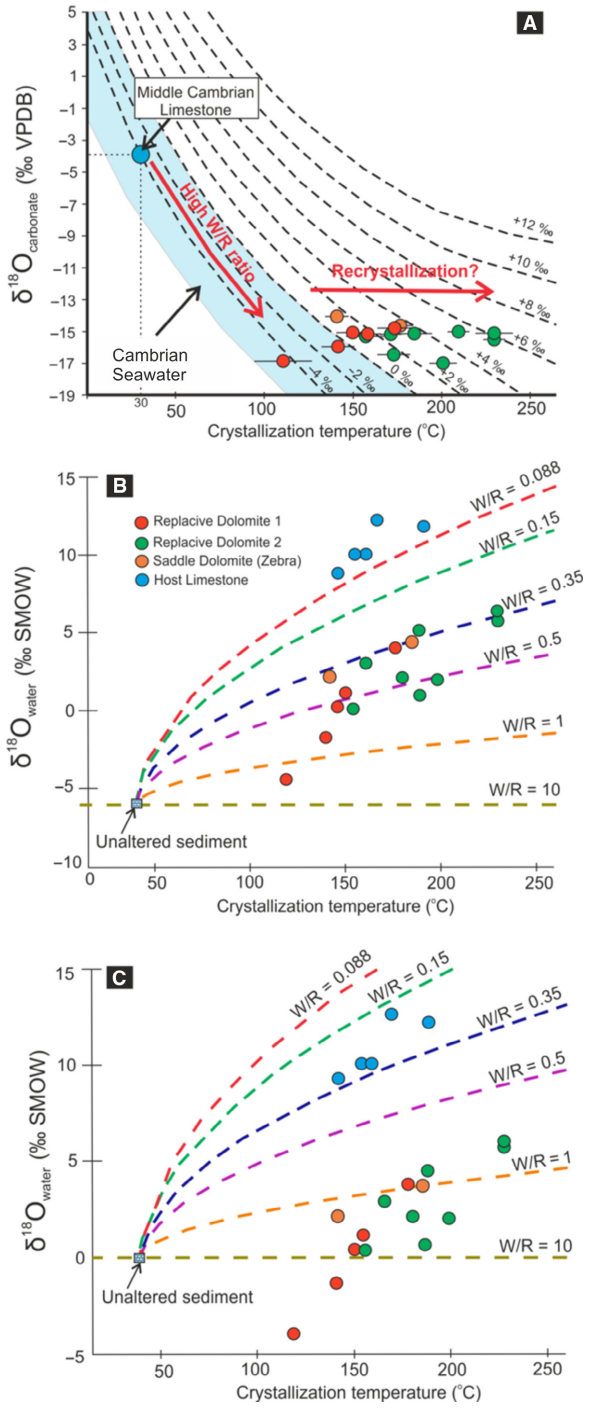

Fig. 11. Recrystallization model and water/rock (W/R) ratio of different dolomite fabrics and limestones (calculation following the method proposed by Banner & Hanson, 1990). (A) Cross-plot between $\delta^{18}O_{dolomite}$ and crystallization temperature. The $\delta^{18}O_{water}$ is following the Horita (2014) equation. (B) and (C) Crystallization model during dolomitization and the corresponding water/rock ratios. (B) uses the Cambrian values suggested by Veizer & Prokoph (2015); and (C) uses the Cambrian values suggested by Henkes *et al.*, 2018 and Ryb & Eiler (2018).

between 146 to 185°C which may suggest that either: (i) the rock has been buried to at least 5 to 6 km, i.e. deeper than previously thought, assuming a normal geothermal gradient; or (ii) a maximum burial depth of 4 km, as suggested by Wright *et al.* (1994). but with a higher geothermal gradient. The latter is feasible because the Mount Whyte Formation was deposited during rifting, when geothermal gradients would have been higher (*ca* 35 to 40°C/km; Bond *et al.*, 1985). Although there is likely to have been a decrease of geothermal gradient during thermal sag subsidence (potentially to 20°C/km; Bertotti *et al.*, 1999), the presence of thick shales above and surrounding the Mount Whyte Formation might have acted as an insulator that retained the high heat flow within the rock sequence (Cercone *et al.*, 1996; Nunn & Lin, 2002).

Temperature of dolomitization

While the fluid inclusion (Th) and Δ_{47} temperatures are broadly similar, they are not totally compatible (Fig. 12) since Δ_{47} temperatures are typically much higher (+10 to 40°C) than the Th temperatures (Fig. 12). Such differences could reflect thermal equilibration of Δ_{47} temperatures through solid-state reordering either by cryptic dissolution or recrystallization (Mangenot *et al.*, 2017). The temperature at which solid-state reordering occurs in dolomite is still not fully understood, but most studies agree that it happens at much slower rates and higher temperatures in dolomite than calcite (Ryb *et al.*, 2017; Lloyd *et al.*, 2018; and references therein) probably >250 to 300°C (Ferry *et al.*, 2011; Ryb *et al.*, 2017). Since Δ_{47} values in calcite the Mount Whyte Formation suggest a temperature of 165°C at maximum burial, the Δ_{47} values for dolomite are most likely not thermally re-equilibrated or altered by solid-state reordering. Hence the values should reflect the crystallization temperature during the dolomitization processes.

Mangenot *et al.* (2017) showed that the temperatures measured by clumped isotope analysis and fluid inclusion analysis generally show a good agreement for temperatures ranging from 70 to 100°C, whether the Th temperatures were pressure corrected or not (Fig. 12). In contrast, different studies of high-temperature dolomite (105 to 175°C) show a similar temperature relationship to that observed in this study (e.g. Came *et al.*, 2017; Honlet *et al.*, 2018), where the majority of the Δ_{47} temperatures are higher than the fluid inclusion

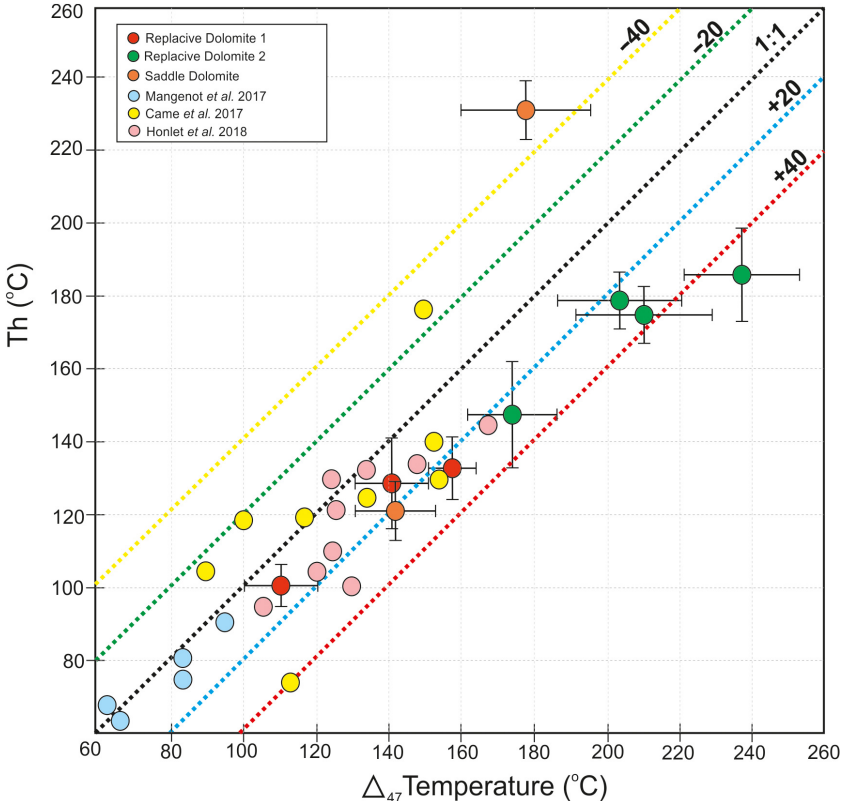

Fig. 12. Comparison between crystallization temperature from fluid inclusion analysis (Th) and clumped isotopes (Δ_{47}) of different dolomite phases in the Mount Whyte Formation. Majority of the samples show higher Δ_{47} temperatures than the Th. Increased in deviation at high temperature is also observed from this cross-plot. The data obtained in this study are also compared with previously published data.

temperatures, even following pressure correction (Fig. 12). In addition, there is also an increase in the deviation between the temperature values at higher temperature (>200°C) (Fig. 12).

While pressure correction (Pc) analysis of the Th could also yield the 'true' entrapment temperature (Tt) (Roedder & Bodnar, 1980), the difficulty in obtaining salinity values in the Mount Whyte Formation (i.e. fluid inclusions did not freeze at the minimum freezing temperature of −180°C) and uncertainty as to the actual pressure regime of the basin, means that pressure correction was not possible. This is potentially further compounded by the interpreted shallow burial depth of dolomitization which creates a relationship between pressure and temperature that is not straightforward. However, if dolomitization in the Mount Whyte and the overlying Cathedral Formation occurred from similar fluids and pressure regime, the fluid salinity (25 wt. % $CaCl_2$) and basin pressure conditions determined by Vandeginste *et al.* (2005) can be used. In this case, the pressure-corrected temperatures calculated using FLUIDS (Bakker, 2009) are +9 to +17°C higher (based on Zhang & Frantz, 1987) than the measured homogenization temperatures, which is still below the Δ_{47} temperatures. In this case, such temperature differences between Th and Δ_{47} may reflect the pressure differences during fluid inclusion entrapment, such that the Th temperatures reflect only the minimum entrapment temperatures whereas the Δ_{47} temperatures show the true entrapment temperatures (Honlet *et al.*, 2018).

Source of magnesium

The origin of dolomitizing fluids in the burial realm has been widely discussed but a suitable source of Mg cannot always be adequately identified (Wilson *et al.*, 1990; Davies & Smith, 2006; Hollis *et al.*, 2017). Utilizing information on the tectonic evolution of the basin, field geometry and different geochemical signals, four possible sources of magnesium-enriched fluids are considered here: (i) dissolved evaporites (for example, chloride and sulphate groups); (ii) fluid the Stephen/Burgess Shale in the distal part of the platform; (iii) seawater; and (iv) crustal fluids.

While dissolved evaporites are often invoked to provide the necessary magnesium for HTD dolomite and to explain the high fluid salinity (Hendry *et al.*, 2015; Martin-Martin *et al.*, 2015;

Koeshidayatullah *et al.*, 2016), the absence of Cambrian, or older, evaporites in the WCSB nullifies the possibility of dissolved evaporites as the main source of magnesium.

If dolomitization took place during shallow burial (<1 km), Mg-rich fluids might have been derived from compactional dewatering of either intraformational Mount Whyte or the Burgess/Stephen shales. Most of the $^{87}Sr/^{86}Sr$ values of the dolomites are beneath the Maximum Sr Isotope Ratio of Basinal Shale (MASIRBAS) value (0.7120; Machel & Cavell, 1999) (Fig. 13B) which may suggest a possible interaction with the shale. However, derivation of large volumes of Mg-enriched brines from normal compaction results in slow flow rates creating only localized dolostone bodies (Drivet & Mountjoy, 1997; Machel & Cavell, 1999). Even during overpressure release, magnesium can be fixed within the shale as chlorite (Frazer *et al.*, 2014). High salinity brines can be derived from shales (Hanor & McIntosh, 2007), but rarely as high as determined in this study. In addition, the maximum burial temperature of the Stephen/Burgess shales when the dolomitization occurred (approximately *ca* 1 to 2 km; Aitken, 1997; Jeary, 2002) would be only around 70–100°C even with an elevated geothermal gradient (>30°C/km), which is much lower than the recorded crystallization temperature.

Seawater is the volumetrically most viable source of water and magnesium, especially when considering the volume of dolostone bodies produced in the Mount Whyte Formation. Furthermore, the presence of high Fe and Mn concentrations, elevated Sr isotope ratios and evolved $\delta^{18}O_{water}$ can be explained by the interaction of seawater with the underlying Cambrian Gog Group (Terreneuvian, Stage 2) or Precambrian Miette Group. This is particularly plausible since dolomitization occurred during shallow burial, when basal sandstone aquifers have been shown to provide important fluid flow pathways for convection of seawater (Martin-Martin *et al.*, 2015; Hollis *et al.*, 2017; Stacey *et al.*, 2018). In addition, the lower range of $\delta^{18}O_{water}$ values of RD1 (Fig. 13A) intersects with the expected upper range of Cambrian seawater. However, there is still much discussion as to the $\delta^{18}O_{water}$ values for Cambrian seawater, in particular whether it was similar to Modern seawater (mean: 0‰ SMOW; Henkes *et al.*, 2018; Ryb & Eiler, 2018) or more negative (mean: −4 to −6‰ SMOW; Veizer & Prokoph, 2015; Vérard & Veizer, 2019). In either case, calculation of $\delta^{18}O_{water}$ for RD2 fabric shows that the mean of isotopic compositions of the dolomitizing fluids are more positive (+2.96‰ SMOW) than Cambrian seawater (Fig. 13A; Table 3). Nevertheless, the lack of a seawater-like REE profile, very high crystallization temperatures and very high fluid salinity (fluid inclusions remained unfrozen at −180°C; e.g. Baldassaro & Bodnar, 2000) of dolomites suggest that there was another significantly hotter and deeper source of fluids. Previous studies of HTD across Canada have proposed fluid interaction with ultramafic rocks (for example, peridotite and serpentinite) and magnesite deposits which have potentially increased the Mg/Ca of dolomitizing fluids (e.g. Powell *et al.*, 2006; Lavoie *et al.*, 2014). More recently, Robertson *et al.* (2019) have demonstrated the significance of carbonation processes of ultramafic rocks [i.e. listwanite – rock consisting of typically magnesite/Mg-bearing carbonate and quartz intergrown with minor fuchsite (Halls & Zhao, 1995; Hansen *et al.*, 2005)] to drive the presence of HTD in Western Canada.

The study area is underlain by complex Palaeometamorphic accreted terranes (Ross *et al.*, 1994), and lithoprobe data taken from around 200 km to the north-east of the study location (Fig. 1B and C) shows the presence of relict of Palaeoproterozoic (1.75 to 1.85 Ga) subduction zone below the WCSB associated with the Snowbird Tectonic Zone (Eaton *et al.*, 1995; Eaton & Cassidy, 1996; Van der Velden & Cook, 2005). The presence of a low velocity zone (LVZ) within this dataset (>12 km depth at present day) has been interpreted to represent ultramafic rocks with a high degree of serpentinization (i.e. subducted serpentinites) (Eaton & Cassidy, 1996) (Fig. 1B). Carbonation of serpentinite (listwanitization) can lead to the formation of Mg-rich minerals, such as magnesite, together with quartz and water. This process has been suggested to sequester large amounts of CO_2 and could also release large volumes of magnesium to drive the formation dolomite (Halls & Zhao, 1995; Scambelluri *et al.*, 2001; Hansen *et al.*, 2005; Schandl & Gorton, 2012; Falk & Kelemen, 2015; Chen *et al.*, 2016; Robertson *et al.*, 2019). Recent work by Robertson *et al.* (2019) indicates that quartz and magnesite precipitation is favoured at <300°C and that CO_2 and H_2S are required to liberate magnesium from ultramafic rocks. These authors also suggested that fluids in equilibrium with magnesite and quartz should have high Mg

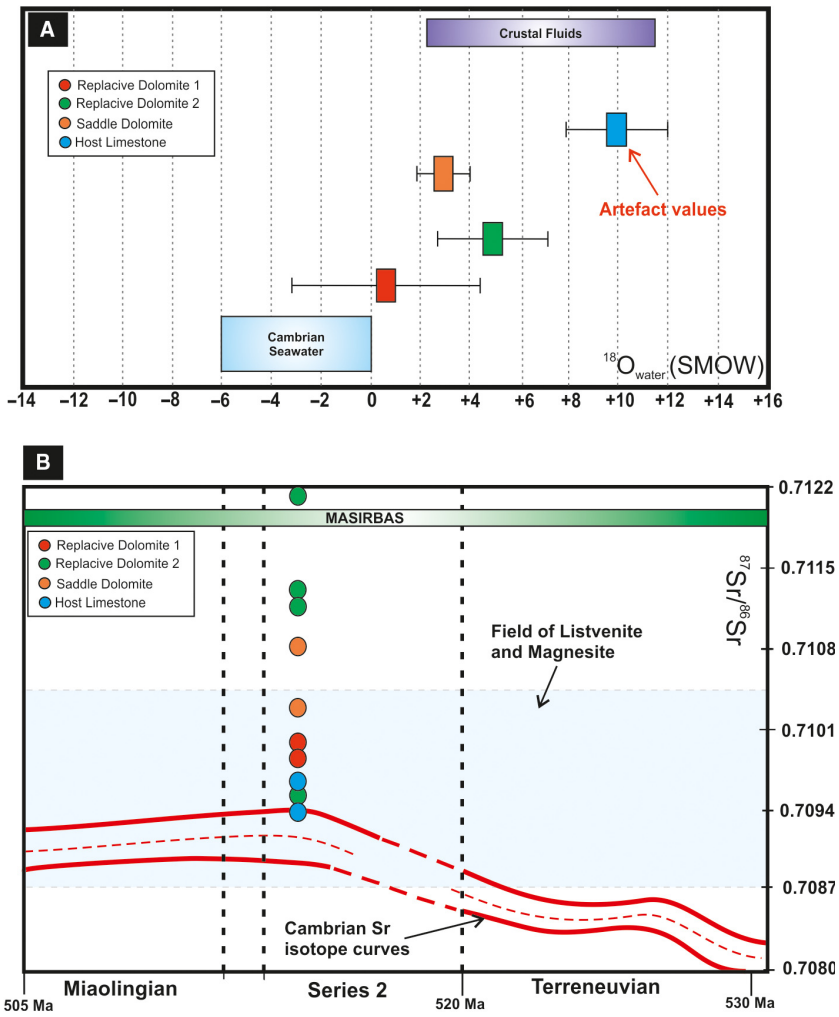

Fig. 13. (A) Variations in the mean of $\delta^{18}O_{water}$ values for the different dolomite phases and host limestone. The values are compared with the Cambrian seawater (Veizer & Prokoph, 2015; Henkes *et al.*, 2018) and crustal fluids (Schulze *et al.*, 2003, and references therein). (B) Enriched $^{87}Sr/^{86}Sr$ ratios of the replacive dolomite phases with respect to the Cambrian $^{87}Sr/^{86}Sr$ values (Montanez *et al.*, 1996). The $^{87}Sr/^{86}Sr$ ratios of the host limestones are fall within and slightly enriched than the expected values. MASIRBAS and listwanite–magnesite values were obtained from Machel & Cavell (1999) and Hinsken *et al.* (2017), respectively.

concentrations. Furthermore, their PHREEQC modelling demonstrates that these fluids not only have a high Mg concentration but also a significantly improved potential to dolomitize limestones due to the modification of Ca^{2+}. Therefore, of the different basement rocks beneath the WCSB, serpentinites and their associated by-products could be considered as a potential source of magnesium and high-temperature fluids for dolomitization in the Mount Whyte Formation.

Trace element analysis of R1 and R2 dolomite in this study has shown a positive Eu anomaly and enrichment of LREE compared to HREE, comparable to the REE profiles of hydrothermal fluids hosted in ultramafic rocks (for example, serpentinites) (Fig. 8A and B; Douville *et al.*, 2002). Dolomite within the Mount Whyte Formation also has high levels of metal enrichment (Table 1), including Fe, Ti and Cr compared to the host limestone, which has also been reported from dolomites associated with ultramafic rocks (Hansen *et al.*, 2005). The positive $\delta^{18}O_{water}$ and radiogenic $^{87}Sr/^{86}Sr$ ratios are also within the range of values derived from carbonated serpentinites and their by-products (for example, magnesite) (Falk & Kelemen, 2015; Hinsken *et al.*, 2017) (Fig. 13A and B). Further supporting evidence comes from the cogenetic relationship between dolomite and quartz in all of the Mount Whyte Formation samples (see XRD data, Koeshidayatullah, 2019) since Schandl & Gorton (2012) and Robertson *et al.* (2019) demonstrated that Mg and Si would be released during the reaction between CO_2-rich fluids and serpentinites. A recent study by Debure *et al.* (2019) has also shown that serpentinization derived brines should have a very high salinity, as observed in this study. Finally, the presence of subducted serpentinites at 5 to

6 km depth beneath the Mount Whyte Formation in the WCSB is in good agreement with the fluid temperatures obtained from Th and Δ_{47} analyses, which were interpreted to have been derived from 5 to 6 km depth, assuming a geothermal gradient of up to 40°C/km.

Nevertheless, carbonation of serpentinites requires interaction with CO_2-rich fluids (Hansen *et al.*, 2005; Falk & Kelemen, 2015; Debure *et al.*, 2019; Robertson *et al.*, 2019) and there is no obvious source of CO_2 for dolomitization during the interpreted period. It is possible that CO_2 was sourced by: (i) degassing during volcanism related to the Terreneuvian to Series 2 Cambrian rifting; or (ii) metamorphism of deeply buried carbonate and clastic strata due to high geothermal gradient. Several studies have reported the presence of mafic and tholeiitic volcanism during the same period as rifting in Western Canada (Stewart, 1972; Cecile *et al.*, 1997; Beranek, 2017; Campbell *et al.*, 2019) and it is possible that CO_2 generated during volcanism could have reacted with the deep-seated serpentinite to liberate large amount of magnesium. Sandiford *et al.* (1998) and Falk & Kelemen (2015) have interpreted CO_2 generation during metasomatism of clastic sediments resulting in enriched $^{87}Sr/^{86}Sr$ values (up to 0.7135), such as observed in the Mount Whyte Formation (Table 3). Since the clastic sediments would have overlain the serpentinites and not been in direct contact with them, however, it is unclear how the CO_2 released by this process, could have caused ultramafic carbonation.

Ultimately, although several lines of geochemical evidence support the interpretation that Mg-rich fluids could have been partially derived from ultramafic rocks, there is no direct evidence of serpentinite beneath the Mount Whyte Formation [i.e. lithoprobe data showing the presence of subducted serpentinites is *ca* 200 km to the north-east of study location (Fig. 1B)]. However, the complex tectonic history of the basin means that the actual underlying stratigraphy – prior to thrusting – is unknown; hence the possibility remains open. The widespread presence of ultramafic–mafic rocks, carbonated serpentinite (listwanite) and their by-products (for example, magnesite) in the WCSB, British Columbia and Eastern Canada (Eaton & Cassidy, 1996; Hansen *et al.*, 2005; Lavoie & Morin, 2004; Lavoie *et al.*, 2014) suggests that ultramafic carbonation could provide an alternative source of magnesium to dolomitizing fluids within the WCSB and beyond. Several studies have reported a close association between dolomite and magnesite mineralization, a common by-product during the carbonation process, in the Cambrian of the WCSB (Nesbitt & Muehlenbachs, 1994; Powell *et al.*, 2006). A recent study by Robertson *et al.* (2019) also discussed the mechanism in which the carbonation process of listwanite sourcing the magnesium for fault-controlled dolomitization in Atlin, British Columbia. Lavoie *et al.* (2014) discussed the presence of hydrothermal dolomitization in Palaeozoic sedimentary strata, Eastern Canada and briefly discussed the possible contribution of Mg-rich ultramafic rocks as a magnesium source of hydrothermal dolomitization. Furthermore, Falk & Kelemen (2015) discussed the presence of dolomite as part of listwanite mineral assemblages in the Samail ophiolite, Jabel Akhdar, Oman, which may indicate the importance of this carbonation process of ultramafic rocks. The widespread presence of HTD in Permian and Jurassic carbonate platforms in the Jabel Akhdar area (Vandeginste *et al.*, 2013; Beckert *et al.*, 2015) may need to be further investigated in order to support the wider application of carbonation of ultramafic rocks in driving the dolomitization process.

Fluid flow model

It has been proposed that RD1 has an isotopic signature that is suggestive of dolomitization from seawater, whilst RD2 is more positive. Strontium isotopic signatures are suggestive of fluid interaction with radiogenic rocks (for example, clastic or basement). Although seawater would have been abundant and able to convect at the proposed burial depths of <1 km, potentially utilizing the basal Gog Group or Miette sandstones as pathways, dolomitization has been shown to occur from very hot, saline fluids that are inconsistent with seawater. Without a confident structural reconstruction of the study area it is not possible to show that it was underlain by serpentinized basement, but it is possible that mixing of deep-seated hydrothermal fluids derived from ultramafic carbonate occurred within the Mount Whyte Formation during convection of seawater in the shallow subsurface, particularly during formation of RD2. This is corroborated by the lower $^{87}Sr/^{86}Sr$ ratios and lower $\delta^{18}O_{water}$ (closer to seawater values) of RD1 than RD2 (Fig. 13B; Table 3). It is possible that these deep-seated, ultramafic-derived brines further increased their Mg/Ca

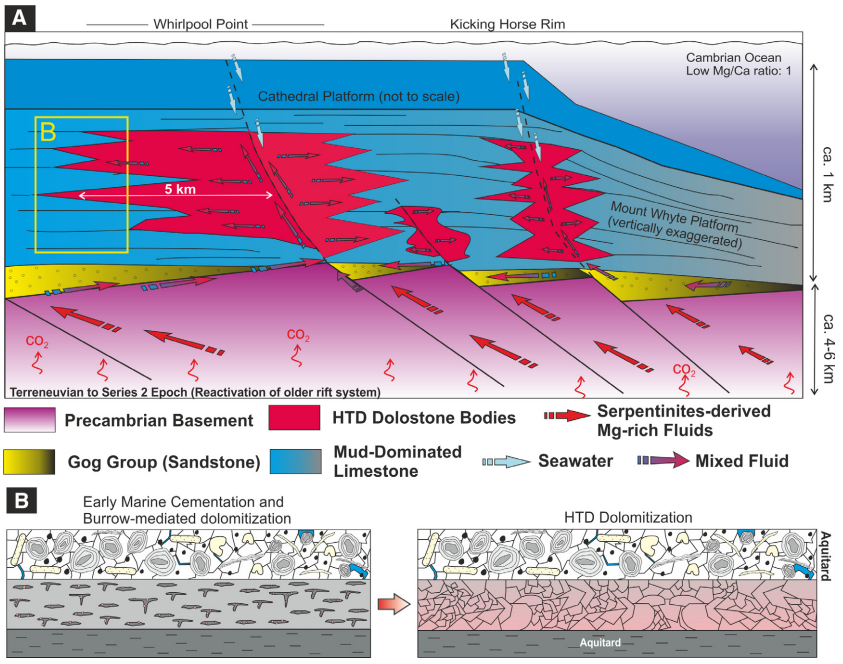

Fig. 14. (A) and (B) Proposed schematic diagrams (not to scale) of hydrothermal dolomitization (HTD) processes in the Mount Whyte Formation. The proposed model shows the depth, timing and possible sources of Mg-rich fluids driving HTD in this formation.

ratio during fluid–rock interaction within the Miette or Gog Groups or by interaction with Mesoproterozoic magnesite, as suggested for the overlying Cathedral Formation (Jeary, 2002; Davies & Smith, 2006; Powell *et al.*, 2006; Stacey *et al.*, 2017). Overall, however, fluid mixing could explain the fact that $^{87}Sr/^{86}Sr$ ratios of RD1 and RD2 are lower than MASIRBAS since previous studies have indicated that interaction between Mg-rich fluids with clastic rocks should have yielded $^{87}Sr/^{86}Sr$ ratios that exceed the MASIRBAS value (Drivet & Mountjoy, 1997; Duggan *et al.*, 2001; Packard *et al.*, 2001). Furthermore, considering the very high salinity and temperature of fluids recorded from both RD1 and RD2 fabrics may suggest that high volumes of fluids were released from deep-seated brines during the coseismic dilatancy pumping associated with Cambrian rifting and mixed with the seawater.

Mechanism and timing of dolomitization

In the Mount Whyte Formation, it has been shown that the dolomitizing fluids were varied in isotopic composition (for example, $\delta^{18}O_{water}$ and $^{87}Sr/^{86}Sr$), very hot and very saline, potentially as a result of mixing between seawater and Mg-enriched fluids supplied from carbonation of deeply seated (*ca* 5 to 6 km) serpentinites at shallow burial depths (<1 km). However, the driving mechanism for fluid flow is not straightforward to unravel due to complex tectonic overprinting, particularly during the Mesozoic Laramide Orogeny that has obscured most of the precursor structural grain. The formation of HTD in the Mount Whyte Formation has been interpreted to involve a large gap between the depth of dolomitization (<1 km) and fluid source (5 to 6 km), and therefore the most likely drive mechanism for fluid migration is tectonic activity, since to transport such deep-seated fluids into the near surface requires high angle, permeable conduits. Since dolomitization is interpreted to have occurred shortly after deposition, during the Cambrian, it could have coincided with Cambrian rifting and thermal subsidence (Powell *et al.*, 2006). Consequently, normal faults would have been dilatant and heat flow high due to ongoing extension (Fig. 14A). Therefore, hot fluids could have been quickly supplied by seismic pumping along faults into the shallow sedimentary succession. This process could have occurred from multiple pulses of large volumes of Mg-rich fluids supplied during coseismic dilatancy.

The interpretation of dolomitization at a shallow depth is corroborated by the alteration of original Cambrian seawater REE and trace element signatures in the dolostone suggest high water/rock ratios during dolomitization. This is in a good agreement with water/rock ratio calculations (Fig. 8A and B) (Banner *et al.*, 1988; Banner & Hanson, 1990). The localization of

dolomitization to bioturbated mudstones is perhaps noteworthy, since although mudstones provide a high reactive surface area, their permeability is typically low (Gabellone & Whitaker, 2016). However, at burial depths of <1 km, the total porosity of the mudstone would still be high (potentially up to 30%; Schmoker & Halley, 1982; Goldhammer, 1997). This condition coupled with the presence of permeability-enhancing burrows may therefore provide sufficient flow pathways for circulation of dolomitizing fluids. Furthermore, organically mediated dolomitization of burrows might have provided 'seeds' that accelerated dolomitization. In contrast, the pervasively cemented grainstone that overlies the dolostone body, and the underlying shale could have focussed fluid flow laterally (Fig. 14B) to form the observed stratabound terminations.

Ultimately, this study provides an unambiguous example of 'true' hydrothermal dolomitization where the fluid temperature is significantly hotter (>150°C) than the ambient rock temperature. In this case, ambient temperature of the host rock should be around 60 to 75°C (based on 35 to 40°C/km geothermal gradient and 35°C surface temperature) while the dolomitization temperature ranges from 120 to 235°C. These recorded crystallization temperatures may have been significantly lower than the actual fluid source temperature due to rapid cooling of fluids during thermal convection and also mixing processes. Therefore, these temperature contrasts (>50°C) have significantly exceeded the temperature difference threshold for hydrothermal dolomitization (>5–10°C; Machel & Lonnee, 2002). The model infers that dolomitization occurred much earlier (Series 2, Stage 3 to stage 5 Cambrian) than previously proposed (for example, Furongian to Cretaceous; Yao & Demicco, 1997; Jeary, 2002; Vandeginste *et al.*, 2005; Davies & Smith, 2006). This earlier timing of dolomitization is supported by Powell *et al.* (2006), who also reported that mobilization of Mg-rich brines along the Kicking Horse area was associated with Cambrian rifting and the observation of large eroded blocks of dolostone that occur within the Stephen/Burgess Shale (Collom *et al.*, 2009).

CONCLUSION

Dolomitization of the Mount Whyte Formation is interpreted to have occurred shortly after deposition, in a shallow burial setting (<1 km), during the late syn-rift. Petrographically, dolomitization in the Mount Whyte Formation is characterized by fabric-destructive dolomite with a wide range of crystal fabrics (RD1, RD2 and SD). All dolomite fabrics are post-dated by bedding-parallel, low amplitude stylolite. These dolomite fabrics also exhibit distinct geochemical signatures compared to the host limestone, including: (i) more negative $\delta^{18}O_{dolomite}$ and more positive $\delta^{18}O_{water}$; (ii) low concentrations of Sr and high Fe and Mn concentrations; (iii) positive Eu anomaly with enriched LREE and depleted HREE. These signatures are suggestive of hydrothermal dolomitizing fluids. Formation temperatures of the dolomite estimated from both Tm and Δ_{47} analyses also indicate a very hot fluid (up to 235°C). Such temperatures, if considering a high geothermal gradient during Cambrian rifting (35 to 40°C/km), should indicate a deep fluid source, potentially from approximately 5 to 6 km depth.

Although aspects of the geochemical fingerprint of RD1 and RD2 dolomite are supportive with dolomitization from heated and modified seawater, high fluid temperatures and salinities are interpreted to potentially reflect a high degree of mixing with Mg-enriched fluids supplied by carbonation of subducted serpentinites below the Western Canada Sedimentary Basin (WCSB). These fluids could have been supplied by seismic pumping during rifting. This interpretation is corroborated by typical ultramafic-derived fluid rare-earth element (REE) patterns, the enrichment of metal concentrations and cogenetic relationship between dolomite and authigenic quartz in the dolomite phases compared to the host limestones. Nevertheless, the complex tectonic history and absence of clear evidence for a source of CO_2 by which carbonation could be initiated means that aspects of this model require further investigation. Ultimately, this study shows that the formation of large-scale hydrothermal dolomitization (HTD) dolostone bodies preferentially took place in shallow burial depth and required multiple pulses and sources of fluids in order to satisfy the mass balance problem.

ACKNOWLEDGEMENTS

University of Manchester provided the funding for AK PhD work through Presidential Doctoral Award. Fieldwork and analytical costs are

supported by a NERC-CDT grant to CH and JS. HR was funded by the PD3 consortium at University of Manchester, supported by Tullow Oil, Woodside Energy and Wintershall DEA. We thank IAS and AAPG postgraduate grants for AK in providing additional support for this study. Help from colleagues at the Williamson Research Centre, University of Manchester, Alberta Geological Survey and Stable Isotope Laboratory, University of Miami, are gratefully acknowledged. We are grateful for the kind support from Matthew Steele-MacInnis and Pillar Lecumberri-Sanchez for the fluid inclusion analysis. Stable isotope analysis was funded through a NERC grant IP-1759-1117 at the NERC Isotope Geoscience Facility in East Kilbride to AB, CH and AK. Anping Hu is acknowledged for the help with strontium isotope analysis. Constructive comments from Editor Giovanna Della Porta, Associate Editor Hairuo Qing, Jeff Lonnee and two anonymous reviewers are greatly acknowledged and have improved the clarity of the paper.

DATA AVAILABILITY STATEMENT

The data that support the findings of this study are available from the corresponding author upon reasonable request.

REFERENCES

Aitken, J.D. (1978) Revised models for depositional grand cycles, Cambrian of Western Canada. *Bull. Can. Pet. Geol.*, **26**, 515–542.

Aitken, J.D. (1989) Birth, growth and death of the Middle Cambrian Cathedral carbonate lithosome, Southern Rocky Mountains. *Bull. Can. Pet. Geol.*, **37**, 316–333.

Aitken, J.D. (1997) Stratigraphy of the Middle Cambrian platformal succession, Southern Rocky mountains. *Geological Survey of Canada Bulletin*, **398**, 322 pp

Al-Aasm, I.S., **Lonnee, J.** and **Clarke, J.** (2002) Multiple fluid flow events and the formation of saddle dolomite: case studies from the Middle Devonian of the Western Canada Sedimentary Basin. *Mar. Pet. Geol.*, **19**, 209–217.

Al-Ramadan, K., **Koeshidayatullah, A.**, **Cantrell, D.** and **Swart, P.K.** (2019). Impact of basin architecture on diagenesis and dolomitization in a fault-bounded carbonate platform: outcrop analogue of a pre-salt carbonate reservoir, Red Sea rift, NW Saudi Arabia. *Petroleum Geoscience*. https://doi.org/10.1144/petgeo2018-125

Amthor, J.E., **Mountjoy, E.W.** and **Machel, H.G.** (1994) Regional-scale porosity and permeability variations in Upper Devonian Leduc buildups: implications for reservoir development and prediction in carbonates. *Am. Asso. Petrol. Geol. Bull.*, **78**, 1541–1558.

Anders, E. and **Grevesse, N.** (1989) Abundances of the elements: Meteoritic and solar. *Geochim. Cosmochim. Acta*, **53**, 197–214.

Aulstead, K.L., **Spencer, R.J.** and **Krouse, H.R.** (1988) Fluid inclusion and isotopic evidence on dolomitization, Devonian of Western Canada. *Geochim. Cosmochim. Acta*, **52**, 1027–1035.

Baadsgaard, H. (1987) Rb-Sr and K-Ca isotope systematics in minerals from potassium horizons in the Prairie Evaporite Formation, Saskatchewan, Canada. *Chem. Geol. Isotope Geosci. sec.*, **66**, 1–15.

Bakker, R.J. (2009) Package FLUIDS. Part 3: correlations between equations of state, thermodynamics and fluid inclusions. *Geofluids*, **9**, 63–74.

Baldassaro, P.M. and **Bodnar, R.J.** (2000) Low temperature phase relations in the system H2O–NaCl–FeCl2: application to fluid inclusion studies. *Geol. Soc. Am. Abs. Prog. A* **A-4**, A-4.

Banner, J.L. and **Hanson, G.N.** (1990) Calculation of simultaneous isotopic and trace element variations during water-rock interaction with applications to carbonate diagenesis. *Geochim. Cosmochim. Acta*, **54**, 3123–3137.

Banner, J.L., **Hanson, G.N.** and **Meyers, W.J.** (1988) Rare earth element and Nd isotopic variations in regionally extensive dolomites from the Burlington-Keokuk Formation (Mississippian); implications for REE mobility during carbonate diagenesis. *J. Sediment. Res.*, **58**, 415–432.

Bau, M. and **Dulski, P.** (1996) Distribution of yttrium and rare-earth elements in the Penge and Kuruman iron-formations, Transvaal Supergroup, South Africa. *Precambr. Res.*, **79**, 37–55.

Beaudoin, N., **Koehn, D.**, **Lacombe, O.**, **Lecouty, A.**, **Billi, A.**, **Aharonov, E.** and **Parlangeau, C.** (2016) Fingerprinting stress: Stylolite and calcite twinning paleopiezometry revealing the complexity of progressive stress patterns during folding—The case of the Monte Nero anticline in the Apennines, Italy. *Tectonics*, **35**, 1687–1712.

Beckert, J., **Vandeginste, V.** and **John, C.M.** (2015) Exploring the geological features and processes that control the shape and internal fabrics of late diagenetic dolomite bodies (Lower Khuff equivalent–Central Oman Mountains). *Mar. Pet. Geol.*, **68**, 325–340.

Beranek, L.P. (2017) A magma-poor rift model for the Cordilleran margin of western North America. *Geology*, **45**, 1115–1118.

Bertotti, G., **Seward, D.**, **Wijbrans, J.**, **Ter Voorde, M.** and **Hurford, A.J.** (1999) Crustal thermal regime prior to, during, and after rifting: a geochronological and modeling study of the Mesozoic South Alpine rifted margin. *Tectonics*, **18**, 185–200.

Bond, G.C. and **Kominz, M.A.** (1984) Construction of tectonic subsidence curves for the early Paleozoic miogeocline, southern Canadian Rocky Mountains: Implications for subsidence mechanisms, age of breakup and crustal thinning. *Geol. Soc. Am. Bull.*, **95**, 155–173.

Bond, G.C., **Christie-Blick, N.**, **Kominz, M.A.** and **Devlin, W.J.** (1985) An Early Cambrian rift to post-rift transition in the Cordillera of western North America. *Nature*, **315**, 742–746.

Brand, U. and **Veizer, J.** (1980) Chemical diagenesis of a multicomponent carbonate system; 1, Trace elements. *J. Sediment. Res.*, **50**, 1219–1236.

Came, R.E., **Azmy, K.**, **Tripati, A.** and **Olanipekun, B.J.** (2017) Comparison of clumped isotope signatures of

dolomite cements to fluid inclusion thermometry in the temperature range of 73–176°C. *Geochim. Cosmochim. Acta*, **199**, 31–47.

Campbell, R.W., **Beranek, L.P.**, **Piercey, S.J.** and **Friedman, R.** (2019) Early Paleozoic post-breakup magmatism along the Cordilleran margin of western North America: New zircon U-Pb age and whole-rock Nd-and Hf-isotope and lithogeochemical results from the Kechika group, Yukon, Canada. *Geosphere*, **15**, 1262–1290.

Cecile, M.P., **Morrow, D.W.** and **Williams, G.K.** (1997) Early Paleozoic (Cambrian to Early Devonian) tectonic framework, Canadian Cordillera. *Bull. Can. Petrol. Geol.*, **45**, 54–74.

Cercone, K.R., **Deming, D.** and **Pollack, H.N.** (1996). Insulating effect of coals and black shales in the Appalachian Basin, western Pennsylvania. *Organic Geochemistry*, **24**(2), 243–249.

Chen, Y.X., **Schertl, H.P.**, **Zheng, Y.F.**, **Huang, F.**, **Zhou, K.** and **Gong, Y.Z.** (2016) Mg–O isotopes trace the origin of Mg-rich fluids in the deeply subducted continental crust of Western Alps. *Earth Planet. Sci. Lett.*, **456**, 157–167.

Collom, C.J., **Johnston, P.A.** and **Powell, W.G.** (2009) Reinterpretation of 'Middle'Cambrian stratigraphy of the rifted western Laurentian margin: Burgess Shale Formation and contiguous units (Sauk II megasequence), Rocky Mountains, Canada. *Palaeogeogr. Palaeoclimatol. Palaeoecol.*, **277**, 63–85.

Corlett, H.J. and **Jones, B.** (2012) Petrographic and geochemical contrasts between calcite-and dolomite-filled burrows in the Middle Devonian Lonely Bay Formation, Northwest Territories, Canada: Implications for dolomite formation in Paleozoic burrows. *J. Sediment. Res.*, **82**, 648–663.

Creaney, S. and **Allan, J.** (1990) Hydrocarbon generation and migration in the Western Canada sedimentary basin. *Geol. Soc. London, Spec. Pub.*, **50**, 189–202.

Craig, H. (1957). Isotopic standards for carbon and oxygen and correction factors for mass-spectrometric analysis of carbon dioxide. *Geochimica et cosmochimica acta*, **12**(1-2), 133–149.

Czerniakowski, L.A., **Lohmann, K.C.** and **Wilson, J.L.** (1984) Closed-system marine burial diagenesis: isotopic data from the Austin Chalk and its components. *Sedimentology*, **31**, 863–877.

Davies, G.R. and **Smith, L.B., Jr** (2006) Structurally controlled hydrothermal dolomite reservoir facies: An overview. *Am. Asso. Petrol. Geol. Bull.*, **90**, 1641–1690.

Debure, M., **Lassin, A.**, **Marty, N.C.**, **Claret, F.**, **Virgone, A.**, **Calassou, S.** and **Gaucher, E.C.** (2019) Thermodynamic evidence of giant salt deposit formation by serpentinization: an alternative mechanism to solar evaporation. *Scientific Reports*, **9**(1), 1–11.

Deiss, C. (1941) Cambrian geography and sedimentation in the central Cordilleran region. *Bull. Geol. Soc. Am.*, **52**, 1085–1115.

Dennis, K.J., **Affek, H.P.**, **Passey, B.H.**, **Schrag, D.P.** and **Eiler, J.M.** (2011) Defining an absolute reference frame for 'clumped'isotope studies of CO2. *Geochim. Cosmochim. Acta*, **75**, 7117–7131.

Deschamps, F., **Godard, M.**, **Guillot, S.** and **Hattori, K.** (2013) Geochemistry of subduction zone serpentinites: A review. *Lithos*, **178**, 96–127.

Dickson, J.A.D. (1966) Carbonate identification and genesis as revealed by staining. *J. Sediment. Res.*, **36**, 491–505.

Douville, E., **Charlou, J.L.**, **Oelkers, E.H.**, **Bienvenu, P.**, **Colon, C.J.**, **Donval, J.P.**, **Fouquet, Y.**, **Prieur, D.** and **Appriou, P.** (2002) The rainbow vent fluids (36 14′ N, MAR): the influence of ultramafic rocks and phase separation on trace metal content in Mid-Atlantic Ridge hydrothermal fluids. *Chem. Geol.*, **184**, 37–48.

Drivet, E. and **Mountjoy, E.W.** (1997) Dolomitization of the Leduc Formation (Upper Devonian), southern Rimbey-Meadowbrook reef trend, Alberta. *J. Sediment. Res.*, **67**, 411–423.

Duggan, J.P., **Mountjoy, E.W.** and **Stasiuk, L.D.** (2001) Fault-controlled dolomitization at Swan Hills Simonette oil field (Devonian), deep basin west-central Alberta, Canada. *Sedimentology*, **48**, 301–323.

Eaton, D.W. and **Cassidy, J.F.** (1996) A relic Proterozoic subduction zone in westüern Canada: New evidence from seismic reflection and receiver function data. *Geophys. Res. Lett.*, **23**, 3791–3794.

Eaton, D.W., **Milkereit, B.**, **Ross, G.M.**, **Kanasewich, E.R.**, **Geis, W.**, **Edwards, D.J.**, **Kelsch, L.** and **Varsek, J.** (1995) Lithoprobe basin-scale seismic profiling in central Alberta: Influence of basement on the sedimentary cover. *Bull. Can. Pet. Geol.*, **43**, 65–77.

Falk, E.S. and **Kelemen, P.B.** (2015) Geochemistry and petrology of listvenite in the Samail ophiolite, Sultanate of Oman: Complete carbonation of peridotite during ophiolite emplacement. *Geochim. Cosmochim. Acta*, **160**, 70–90.

Ferry, J.M., **Passey, B.H.**, **Vasconcelos, C.** and **Eiler, J.M.** (2011) Formation of dolomite at 40–80°C in the Latemar carbonate buildup, Dolomites, Italy, from clumped isotope thermometry. *Geology*, **39**, 571–574.

Frazer, M., **Whitaker, F.** and **Hollis, C.** (2014). Fluid expulsion from overpressured basins: Implications for Pb–Zn mineralisation and dolomitization of the East Midlands platform, Northern England. *Marine and Petroleum Geology*, **55**, 68–86.

Gabellone, T. and **Whitaker, F.** (2016) Secular variations in seawater chemistry controlling dolomitization in shallow reflux systems: insights from reactive transport modelling. *Sedimentology*, **63**, 1233–1259.

Gabrielse, H., **Monger, J.W.H.**, **Wheeler, J.O.** and **Yorath, C.J.** (1991) Morphogeological belts, tectonic assemblages, and terranes. Geology of the Cordilleran Orogen in Canada. Edited by H. Gabrielse and CJ Yorath. *Geol. Survey Canada, Geol. Canada*, **4**, 15–28.

Ghosh, P., **Adkins, J.**, **Affek, H.**, **Balta, B.**, **Guo, W.**, **Schauble, E.A.**, **Schrag, D.** and **Eiler, J.M.** (2006) 13C–18O bonds in carbonate minerals: a new kind of paleothermometer. *Geochim. Cosmochim. Acta*, **70**, 1439–1456.

Gingras, M.K., **Pemberton, S.G.**, **Muelenbachs, K.** and **Machel, H.** (2004) Conceptual models for burrow-related, selective dolomitization with textural and isotopic evidence from the Tyndall Stone, Canada. *Geobiology*, **2**, 21–30.

Goldhammer, R.K. (1997) Compaction and decompaction algorithms for sedimentary carbonates. *J. Sediment. Res.*, **67**, 26–35.

Goldstein, R.H. and **Reynolds, T.J.** (1994) *Systematics of Fluid Inclusions in Diagenetic Minerals*. SEPM Short Course 31, SEPM, Oklahoma, Tulsa.

Halls, C. and **Zhao, R.** (1995) Listvenite and related rocks: perspectives on terminology and mineralogy with reference to an occurrence at Cregganbaun, Co., Mayo, Republic of Ireland. *Miner. Deposita*, **30**, 303–313.

Hanor, J.S. and **McIntosh, J.C.** (2007) Diverse origins and timing of formation of basinal brines in the Gulf of Mexico sedimentary basin. *Geofluids*, **7**(2), 227–237.

Hansen, L.D., **Dipple, G.M.**, **Gordon, T.M.** and **Kellett, D.A.Ü.** (2005) Carbonated serpentinite (listwanite) at Atlin, British Columbia: A geological analogue to carbon dioxide sequestration. *Can. Mineral.*, **43**, 225–239.

Hendry, J.P., **Gregg, J.M.**, **Shelton, K.L.**, **Somerville, I.D.** and **Crowley, S.F.** (2015) Origin, characteristics and distribution of fault-related and fracture-related dolomitization: Insights from Mississippian carbonates, Isle of Man. *Sedimentology*, **62**, 717–752.

Henkes, G.A., **Passey, B.H.**, **Grossman, E.L.**, **Shenton, B.J.**, **Yancey, T.E.** and **Pérez-Huerta, A.** (2018) Temperature evolution and the oxygen isotope composition of Phanerozoic oceans from carbonate clumped isotope thermometry. *Earth Planet. Sci. Lett.*, **490**, 40–50.

Hinsken, T., **Bröcker, M.**, **Strauss, H.** and **Bulle, F.** (2017) Geochemical, isotopic and geochronological characterization of listvenite from the Upper Unit on Tinos, Cyclades, Greece. *Lithos*, **282**, 281–297.

Hirani, J., **Bastesen, E.**, **Boyce, A.**, **Corlett, H.**, **Gawthorpe, R.**, **Hollis, C.**, **John, C.M.**, **Robertson, H.**, **Rotevatn, A.** and **Whitaker, F.** (2018) Controls on the formation of stratabound dolostone bodies, Hammam Faraun Fault block, Gulf of Suez. *Sedimentology*, **65**, 1973–2002.

Hollis, C., **Bastesen, E.**, **Boyce, A.**, **Corlett, H.**, **Gawthorpe, R.**, **Hirani, J.**, **Rotevatn, A.** and **Whitaker, F.** (2017) Fault-controlled dolomitization in a rift basin. *Geology*, **45**, 219–222.

Honlet, R., **Gasparrini, M.**, **Muchez, P.**, **Swennen, R.** and **John, C.M.** (2018) A new approach to geobarometry by combining fluid inclusion and clumped isotope thermometry in hydrothermal carbonates. *Terra Nova*, **30**, 199–206.

Horita, J. (2014) Oxygen and carbon isotope fractionation in the system dolomite–water–CO2 to elevated temperatures. *Geochim. Cosmochim. Acta*, **129**, 111–124.

Horita, J., **Zimmermann, H.** and **Holland, H.D.** (2002) Chemical evolution of seawater during the Phanerozoic: Implications from the record of marine evaporites. *Geochim. Cosmochim. Acta*, **66**, 3733–3756.

Ishihara, S., **Hua, R.**, **Hoshino, M.** and **Murakami, H.** (2008) REE abundance and REE minerals in granitic rocks in the Nanling range, Jiangxi Province, southern China, and generation of the REE-rich weathered crust deposits. *Res. Geol.*, **58**, 355–372.

Jeary, V.A. (2002). *The origin of middle Cambrian-hosted mid-platform dolomite; Cathedral Formation, Whirlpool Point, Alberta*. Unpublished MSc thesis. University of Calgary, Calgary, AB.

Kim, S.T. and **O'Neil, J.R.** (1997) Equilibrium and nonequilibrium oxygen isotope effects in synthetic carbonates. *Geochim. Cosmochim. Acta*, **61**, 3461–3475.

Koeshidayatullah, A. (2019) *Determination of the Processes Governing the Termination of Fault-Controlled Dolostone Bodies*. PhD Thesis. University of Manchester, Manchester.

Koeshidayatullah, A., **Al-Ramadan, K.**, **Collier, R.** and **Hughes, G.W.** (2016) Variations in architecture and cyclicity in fault-bounded carbonate platforms: Early Miocene Red Sea Rift, NW Saudi Arabia. *Mar. Pet. Geol.*, **70**, 77–92.

Kubli, T. and **Simony, P.S.** (1994) The Dogtooth Duplex, a model for the structural development of the northern Purcell Mountains. *Can. J. Earth Sci.*, **31**, 1672–1686.

Land, L.S. (1980) The isotopic and trace element geochemistry of dolomite: the state of the art. In: *Concepts and Models of Dolomitization* (Eds Zenger, D.H., Dunham, J.B., and Ethington, R.L.). Spec. Publ.-SEPM, Oklahoma, **28**, 87–110.

Lavoie, D. and **Morin, C.** (2004) Hydrothermal dolomitization in the Lower Silurian Sayabec Formation in northern Gaspé-Matapédia (Québec): Constraint on timing of porosity and regional significance for hydrocarbon reservoirs. *Bull. Can. Pet. Geol.*, **52**, 256–269.

Lavoie, D., **Chi, G.**, **Brennan-Alpert, P.**, **Desrochers, A.** and **Bertrand, R.** (2005) Hydrothermal dolomitization in the Lower Ordovician Romaine Formation of the Anticosti Basin: significance for hydrocarbon exploration. *Bull. Can. Pet. Geol.*, **53**, 454–471.

Lavoie, D., **Jackson, S.** and **Girard, I.** (2014) Magnesium isotopes in high-temperature saddle dolomite cements in the lower Paleozoic of Canada. *Sed. Geol.*, **305**, 58–68.

Lawson, M., **Shenton, B.J.**, **Stolper, D.A.**, **Eiler, J.M.**, **Rasbury, E.T.**, **Becker, T.P.**, **Phillips-Lander, C.M.**, **Buono, A.S.**, **Becker, S.P.**, **Pottorf, R.** and **Gray, G.G.** (2018) Deciphering the diagenetic history of the El Abra Formation of eastern Mexico using reordered clumped isotope temperatures and U-Pb dating. *Geol. Soc. Am. Bull.*, **130**, 617–629.

Lloyd, M.K., **Ryb, U.** and **Eiler, J.M.** (2018) Experimental calibration of clumped isotope reordering in dolomite. *Geochim. Cosmochim. Acta*, **242**, 1–20.

Machel, H.G. (2004) Concepts and models of dolomitization: A critical reappraisal. In: *The Geometry and Petrogenesis of Dolomite Hydrocarbon Reservoirs* (Eds Braithwaite, C.J.R., Rizzi, G. and Darke, G.), *Geological Society of London Special Publication*, **235**, 7–63.

Machel, H.G. and **Cavell, P.A.** (1999) Low-flux, tectonically-induced squeegee fluid flow. *Bull. Can. Pet. Geol.*, **47**, 510–533.

Machel, H.G. and **Lonnee, J.** (2002) Hydrothermal dolomite —A product of poor definition and imagination. *Sed. Geol.*, **152**, 163–171.

Mangenot, X., **Bonifacie, M.**, **Gasparrini, M.**, **Götz, A.**, **Chaduteau, C.**, **Ader, M.** and **Rouchon, V.** (2017) Coupling Δ47 and fluid inclusion thermometry on carbonate cements to precisely reconstruct the temperature, salinity and δ18O of paleo-groundwater in sedimentary basins. *Chem. Geol.*, **472**, 44–57.

Martin-Martin, J.D., **Travé, A.**, **Gomez-Rivas, E.**, **Salas, R.**, **Sizun, J.P.**, **Vergés, J.**, **Corbella, M.**, **Stafford, S.L.** and **Alfonso, P.** (2015) Fault-controlled and stratabound dolostones in the Late Aptian–earliest Albian Benassal Formation (Maestrat Basin, E Spain): Petrology and geochemistry constrains. *Mar. Pet. Geol.*, **65**, 83–102.

McCrea, J.M. (1950) On the isotopic chemistry of carbonates and a paleotemperature scale. *J. Chem. Phys.*, **18**, 849–857.

McLennan, S.M. (1989) Rare earth elements in sedimentary rocks: Influence of provenance and sedimentary processes. In: *Geochemistry and Mineralogy of Rare Earth Elements* (Eds Lipin, B.R. and McKay, G.A.), pp. 169–200. *Mineralogical Society of America*, Virginia.

Montañez, I.P., **Banner, J.L.**, **Osleger, D.A.**, **Borg, L.E.** and **Bosserman, P.J.** (1996) Integrated Sr isotope variations and sea-level history of Middle to Upper Cambrian platform carbonates: Implications for the evolution of Cambrian seawater 87Sr/86Sr. *Geology*, **24**, 917–920.

Mountjoy, E.W., **Machel, H.G.**, **Green, D.**, **Duggan, J.** and **Williams-Jones, A.E.** (1999) Devonian matrix dolomites and deep burial carbonate cements: a comparison between the Rimbey-Meadowbrook reef trend and the deep basin of west-central Alberta. *Bull. Can. Pet. Geol.*, **47**, 487–509.

Murray, S.T., **Arienzo, M.M.** and **Swart, P.K.** (2016) Determining the Δ47 acid fractionation in dolomites. *Geochim. Cosmochim. Acta*, **174**, 42–53.

Nesbitt, B.E. and **Muehlenbachs, K.** (1994) Paleohydrogeology of the Canadian Rockies and origins of brines, Pb-Zn deposits and dolomitization in the Western Canada Sedimentary Basin. *Geology*, **22**, 243–246.

Norford, B. S. (2012) Middle Cambrian–Middle Ordovician rocks of western Canada, latitude 49° to the Peace River. In: *The great American carbonate bank: The geology and economic resources of the Cambrian–Ordovician Sauk megasequence of Laurentia* (Eds Derby, J.R., Fritz, R.D., Longacre, S.A., Morgan, W.A and Sternbach, C.A.), AAPG Memoir, Oklahoma, **98**, 725–734.

Nunn, J.A. and **Lin, G.** (2002) Insulating effect of coals and organic rich shales: implications for topography-driven fluid flow, heat transport, and genesis of ore deposits in the Arkoma Basin and Ozark Plateau. *Basin Research*, **14**(2), 129–145.

Packard, J.J., **Al-Aasm, I.**, **Samson, I.**, **Berger, Z.** and **Davies, J.** (2001) A Devonian hydrothermal chert reservoir: the 225 bcf Parkland field, British Columbia, Canada. *Am. Asso. Petrol. Geol. Bull.*, **85**, 51–84.

Passey, B.H. and **Henkes, G.A.** (2012) Carbonate clumped isotope bond reordering and geospeedometry. *Earth Planet. Sci. Lett.*, **351**, 223–236.

Powell, W.G., **Johnston, P.A.**, **Collom, C.J.** and **Johnston, K.J.** (2006) Middle Cambrian brine seeps on the Kicking Horse Rim and their relationship to talc and magnesite mineralization and associated dolomitization, British Columbia, Canada. *Econ. Geol.*, **101**, 431–451.

Qing, H. and **Mountjoy, E.W.** (1994) Rare earth element geochemistry of dolomites in the Middle Devonian Presqu'ile barrier, Western Canada Sedimentary Basin: implications for fluid-rock ratios during dolomitization. *Sedimentology*, **41**, 787–804.

Radke, B.M. and **Mathis, R.L.** (1980) On the formation and occurrence of saddle dolomite. *J. Sediment. Petrol*, **504**, 1149–1168.

Robertson, H., **Corlett, H.**, **Hollis, C.**, **Kibblewhite, T.** and **Whitaker, F.** (2019) Listwanitization as a source of Mg for dolomitization: field evaluation in Atlin, British Columbia. Goldschmidt Conference, Barcelona, August 2019.

Roedder, E. and **Bodnar, R.J.** (1980) Geologic pressure determinations from fluid inclusion studies. *Annu. Rev. Earth Planet. Sci.*, **8**, 263–301.

Rosenbaum, J. and **Sheppard, S.M.F.** (1986) An isotopic study of siderites, dolomites and ankerites at high temperatures. *Geochim. Cosmochim. Acta*, **50**, 1147–1150.

Ross, G.M., **Broome, J.** and **Miles, W.** (1994) Potential Fields and Basement Structure. In: *Geological atlas of the western Canada sedimentary basin* (Ed. Mossop, G.D. and Shetsen, I.), *Canadian Society of Petroleum Geologists and the Alberta Research Council Calgary*, Alberta, 41.

Ryb, U. and **Eiler, J.M.** (2018) Oxygen isotope composition of the Phanerozoic ocean and a possible solution to the dolomite problem. *Proc. Natl Acad. Sci. USA*, **115**, 6602–6607.

Ryb, U., **Lloyd, M.K.**, **Stolper, D.A.** and **Eiler, J.M.** (2017) The clumped-isotope geochemistry of exhumed marbles from Naxos, Greece. *Earth Planet. Sci. Lett.*, **470**, 1–12.

Sandiford, M., **Hand, M.** and **McLaren, S.** (1998) High geothermal gradient metamorphism during thermal subsidence. *Earth Planet. Sci. Lett.*, **163**, 149–165.

Scambelluri, M., **Rampone, E.** and **Piccardo, G.B.** (2001) Fluid and element cycling in subducted serpentinite: a trace-element study of the Erro-Tobbio high pressure ultramafites (Western Alps, NW Italy). *J. Petrol.*, **42**, 55–67.

Schandl, E.S. and **Gorton, M.P.** (2012) Hydrothermal alteration and CO2 metasomatism (natural carbon sequestration) of komatiites in the south-western Abitibi greenstone belt. *Can. Mineral.*, **50**, 129–146.

Schmoker, J.W. and **Halley, R.B.** (1982) Carbonate porosity versus depth: a predictable relation for south Florida. *Am. Asso. Petrol. Geol. Bull.*, **66**, 2561–2570.

Schulze, D.J., **Harte, B.**, **Valley, J.W.**, **Brenan, J.M.** and **Dominic, M.D.R.** (2003) Extreme crustal oxygen isotope signatures preserved in coesite in diamond. *Nature*, **423**, 68–70.

Sharma, T. and **Clayton, R.N.** (1965) Measurement of O18O16 ratios of total oxygen of carbonates. *Geochim. Cosmochim. Acta*, **29**, 1347–1353.

Sibley, D.F. and **Gregg, J.M.** (1987) Classification of dolomite rock textures. *J. Sediment. Res.*, **57**, 967–975.

Slind, O.L., **Andrews, G.D.**, **Murray, D.L.**, **Norford, B.S.**, **Paterson, D.F.**, **Salas, C.J.** and **Tawadros, E.E.** (1994). Middle Cambrian to Lower Ordovician strata of the Western Canada Sedimentary Basin. In: *Geological Atlas of the Western Canada Sedimentary Basin* (Eds. Mossop, G. and Shetsen, I.), *Canadian Society of Petroleum Geologists and Alberta Research Council, Special Report*, **4**, 87–108.

Stacey, J., **Koeshidayatullah, A.**, **Hollis, C.** and **Corlett, H.** (2017) Multistage fault-related dolomitization of the Middle Cambrian Mount Whyte and Cathedral formations: Insights into tectonic and diagenetic history of the Western Canada Sedimentary Basin. AAPG ICE 2017.

Staudigel, P.T., **Murray, S.**, **Dunham, D.P.**, **Frank, T.D.**, **Fielding, C.R.** and **Swart, P.K.** (2018) Cryogenic brines as diagenetic fluids: Reconstructing the diagenetic history of the Victoria Land Basin using clumped isotopes. *Geochim. Cosmochim. Acta*, **224**, 154–170.

Stewart, J.H. (1972) Initial deposits in the Cordilleran geosyncline: Evidence of a late Precambrian (<850 my) continental separation. *Geol. Soc. Am. Bull.*, **83**, 1345–1360.

Swart, P.K. (2015) The geochemistry of carbonate diagenesis: The past, present and future. *Sedimentology*, **62**, 1233–1304.

Swart, P.K., **Cantrell, D.L.**, **Arienzo, M.M.** and **Murray, S.T.** (2016) Evidence for high temperature and 18O-enriched fluids in the Arab-D of the Ghawar Field, Saudi Arabia. *Sedimentology*, **63**, 1739–1752.

Tremblay, V.J. (1996) Trilobites and strata of the Lower and Middle Cambrian Peyto, Mount Whyte and Naiset formations, Alberta and British Columbia. *Unpublished PhD Thesis*. 344.

Van der Velden, A.J. and **Cook, F.A.** (2005) Relict subduction zones in Canada. *J. Geophys. Res. Solid Earth*, **110**, 1–17.

Vandeginste, V., **Swennen, R.**, **Gleeson, S.A.**, **Ellam, R.M.**, **Osadetz, K.** and **Roure, F.** (2005) Zebra Dolomitization as a result of focused fluid flow in the Rocky Mountains Fold and Thrust Belt, Canada. *Sedimentology*, **52**, 1067–1095.

Vandeginste, V., **John, C.M.**, **van de Flierdt, T.** and **Cosgrove, J.W.** (2013) Linking process, dimension, texture, and geochemistry in dolomite geobodies: A case study from Wadi Mistal (northern Oman) linking process, dimension, texture, and geochemistry in dolomite geobodies. *Am. Asso. Petrol. Geol. Bull.*, **97**, 1181–1207.

Veizer, J. (1983). Trace elements and isotopes in sedimentary carbonates. In: *Carbonates: Mineralogy and Chemistry* (Ed. Reeder, R.J.), *Mineralogical Society of America: Review Mineral*, **11**, 265–300.

Veizer, J. and **Prokoph, A.** (2015) Temperatures and oxygen isotopic composition of Phanerozoic oceans. *Earth Sci. Rev.*, **146**, 92–104.

Vérard, C. and **Veizer, J.** (2019) On plate tectonics and ocean temperatures. *Geology*, **47**, 881–885.

Wallace, M.W., **Shuster, A.**, **Greig, A.**, **Planavsky, N.J.** and **Reed, C.P.** (2017) Oxygenation history of the Neoproterozoic to early Phanerozoic and the rise of land plants. *Earth Planet. Sci. Lett.*, **466**, 12–19.

Webb, G.E. and **Kamber, B.S.** (2000) Rare earth elements in Holocene reefal microbialites: a new shallow seawater proxy. *Geochim. Cosmochim. Acta*, **64**, 1557–1565.

Weides, S. and **Majorowicz, J.** (2014) Implications of spatial variability in heat flow for geothermal resource evaluation in large foreland basins: the case of the Western Canada Sedimentary Basin. *Energies*, **7**, 2573–2594.

Wilson, E.N., **Hardie, L.A.** and **Phillips, O.M.** (1990) Dolomitization front geometry, fluid flow patterns, and the origin of massive dolomite: the Triassic Latemar buildup, northern Italy. *Am. J. Sci.*, **290**, 741–796.

Winkelstern, I.Z. and **Lohmann, K.C.** (2016) Shallow burial alteration of dolomite and limestone clumped isotope geochemistry. *Geology*, **44**, 467–470.

Wright, G.N., **McMechan, M.E.**, **Potter, D.E.G.**, **Mossop, G.D.** and **Shetsen, I.** (1994) Structure and architecture of the Western Canada sedimentary basin. *Geol. Atlas West. Can. Sediment. Basin*, **4**, 25–40.

Yao, Q. and **Demicco, R.V.** (1997) Dolomitization of the Cambrian carbonate platform, southern Canadian Rocky Mountains; dolomite front geometry, fluid inclusion geochemistry, isotopic signature, and hydrogeologic modelling studies. *Am. J. Sci.*, **297**, 892–938.

Zhang, Y.G. and **Frantz, J.D.** (1987) Determination of the homogenization temperatures and densities of supercritical fluids in the system $NaClKClCaCl_2H_2O$ using synthetic fluid inclusions. *Chem. Geol.*, **64**, 335–350.

Manuscript received 16 May 2019; revision accepted 6 March 2020